A Statistical description of concurrent mixing and crystallisation during MORB differentiation: Implications for trace element enrichment

Oliver Shorttle[a,b], John F Rudge[b], John Maclennan[b], Ken H Rubin[c]

[a]*Division of Geological and Planetary Sciences, California Institute of Technology, Pasadena, California, USA*
[b]*Department of Earth Sciences, University of Cambridge, Downing Street, Cambridge CB2 3EQ, UK*
[c]*Department of Geology and Geophysics, SOEST, University of Hawaii, 1680 East West Road, Honolulu, HI 96822*

Abstract

The pattern of trace element enrichment and variability found in differentiated suites of basalts is a simple observable, which nonetheless records a wealth of information on processes occurring from the mantle to crustal magma chambers. The incompatible element contents of some mid-ocean ridge basalt (MORB) sample suites show progressive enrichment beyond the predictions of simple models of fractional crystallisation of a single primary melt. Explanations for this over-enrichment have focused on the differentiation processes in crustal magma chambers. In this paper we consider an additional mechanism, and focus instead on the deviation from simple fractionation trends that is possible by mixing of diverse mantle-derived melts supplied to magma chambers. A primary observation motivating this strategy is that there is significant chemical diversity in primitive high MgO basalts, which single liquid parent models cannot match. Models were developed to simulate the compositional effects of concurrent mixing and crystallisation (CMC): diverse parental melts were allowed to mix, with a likelihood that is proportional to the extent of fractional crystallisation. Using a simple statistical model to explore the effects of concurrent mixing and crystallisation on apparent liquid lines of descent, we show how significant departure from Rayleigh fractionation is possible as a function of the diversity of trace elements in the incoming melts, their primary MgO, and the relative proportion of enriched to depleted melts.

The model was used to make predictions of gradients of trace element enrichment in log[trace element]–MgO space. These predictions were compared with observations from a compilation of global MORB and provide a test of the applicability of CMC to natural systems. We find that by considering the trace element variability of primitive MORB, its MgO content and degree of enrichment, CMC accurately predicts the pattern of trace element over-enrichment seen in global MORB. Importantly, this model shows that the relationship between over-enrichment and incompatibility can derive from mantle processes: the fact that during mantle melting maximum variability is generated in those elements with the smallest bulk K_d. Magma chamber processes are therefore filtering the signal of mantle-derived chemical diversity to produce trace element over-enrichment during differentiation.

Finally, we interrogate the global MORB dataset for evidence that trace element over-enrichment varies as a function of melt supply. There is no correlation between over-enrichment and melt supply in the global dataset. Trace element over-enrichment occurs at slow-spreading ridges where extensive steady-state axial magma chambers, the most likely environment for repeated episodes of replenishment, tapping and crystallisation, are very rarely detected. This supports a model whereby trace element over-enrichment is an inevitable consequence of chemically heterogeneous melts delivered from the mantle, a process that may operate across all rates of melt supply.

Keywords: Concurrent mixing and crystallisation, MORB, Magmatic differentiation, Magma mixing, Mantle heterogeneity

Introduction

The supply of basaltic magma to mid-ocean ridges and its subsequent low pressure evolution is a fundamental part of solid-Earth geochemical cycling, which supplies heat and nutrients to the surface environment, and sequesters water and other elements for return to the mantle (Elderfield and Schultz, 1986; Parai and Mukhopadhyay, 2012). The magmatic processes which drive this cycling are collectively termed differentiation (Bowen, 1915), the essential trajectory of which is the loss of heat and mass from primitive mantle derived magmas. The importance of this for mid-ocean ridge basalts (MORB) was demonstrated by O'Hara (1968), who showed that MORB must have been driven out of equilibrium with their mantle sources by low pressure crystallisation.

We can gain insight into how differentiation proceeds by studying the composition of basalts erupted at various stages of the differentiation process. Compatible elements such as MgO, which in basaltic magmas undergo near monotonic decrease over the majority of their crystallisation interval, provide an index of magmatic differentiation. Incompatible trace elements, which are excluded from the fractionating assemblage of olivine±plagioclase±clinopyroxene, increase in concentration with progressive differentiation. In combination, these observables provide a powerful tool for assessing the rate of mass loss during differentiation, and the details of magma chamber processes.

Possibly the simplest description of magmatic differentiation is as a Rayleigh fractionation-type process

$$C = C_0(1 - X)^{(K_d - 1)}, \tag{1}$$

whereby the concentration of an element C in a magma derivative to a parental melt with composition C_0, is a function of the mass loss due to crystallisation X, and the distribution coefficient K_d between the melt and bulk crystallising assemblage. This model would predict an increase in incompatible element contents inversely proportional to the degree of crystallisation, with a limit on the enrichment of a trace element of $C \leq C_0/(1 - X)$. Taking the log of equation 1 we can define a similar limit in terms of the maximum mean gradient of trace element enrichment over the differentiation interval, $d(\log[C])/d(\mathrm{MgO})|_{\max}$, as

$$d(\log[C])/d(\mathrm{MgO})|_{\max} = \log_{10}\left[1 - X_{\max}\right]/(\mathrm{MgO}_{\max} - \mathrm{MgO}_{\min}). \tag{2}$$

Despite the appealing simplicity of fractional crystallisation, magmatic differentiation, as noted by Bowen, "...*has been much discussed and apparently every conceivable process given a place as a factor in producing the observed results*" (Bowen, 1915). The century following Bowen's comment has continued in much the same spirit, with fractional crystallisation being challenged as a net descriptor of magmatic differentiation because, amongst other reasons, in some basalt suites it can not explain the observed rate of trace element enrichment during crystallisation (i.e. gradients are found steeper than $d(\log[C])/d(\mathrm{MgO})|_{\max}$, Fig. 1 and Bryan et al. (1976)). This observation of trace element over-enrichment has led to a range of models elaborating upon magmatic differentiation processes to include: (1) chromatographic fractionation of trace elements in magmas as they migrate up through crystal piles (Coogan et al., 2000b; Lissenberg et al., 2013); (2) repeated episodes of magma replenishment, tapping and crystallisation achieving a steady state magma chamber enriched in incompatible elements at a given MgO (O'Hara, 1977; O'Hara and Matthews, 1981; Albarède, 1985; O'Neill and Jenner, 2012); and (3) in situ crystallisation mechanisms, whereby evolved liquids in boundary layers or mushes contribute to magma chamber evolution (Langmuir, 1989; Coogan and O'Hara, 2015).

The models mentioned above, including those recent versions renewing this debate (O'Neill and Jenner, 2012; Coogan and O'Hara, 2015), have all investigated trace element over-enrichment in the context of crustal processes not captured by the Rayleigh fractionation of equation 1. Whilst we consider this a reasonable approach to take, we think there is also merit in pursuing an alternative hypothesis: that magmatic differentiation processes are (nearly) as simple as Rayleigh fractionation, but that the diverse chemistry of melts supplied from the mantle causes local and global trends of trace element over-enrichment. Our alternative hypothesis is founded on the observation that at high MgO there is abundant chemical variability in magmas, which mixing will systematically erase (e.g. Shorttle (2015)). This primary variability is overlooked, or considered of secondary importance, in repeated replenishment-type models, but is a feature of global

MORB that enables apparent liquid lines of descent to deviate from simple fractional crystallisation. Such mantle-derived chemical heterogeneity will exist because: (1) mantle melting is a near-fractional process (Johnson et al., 1990); (2) near-fractional melting will generate a wide range of melt compositions, even when the mantle source is homogeneous in its trace element composition (e.g. Fig. 2, and Langmuir et al. (1977)); and (3), melts out of major and trace element equilibrium with their matrix can survive transport through the mantle (Spiegelman and Kelemen, 2003) and enter crustal and upper mantle magma chambers (Sobolev, 1996). Any heterogeneity in the mantle source will add to these effects.

Accepting these points, our model only extends Rayleigh fractionation of magmas to include mixing between these heterogeneous mantle melts, with a probability proportional to their degree of differentiation. This process is termed concurrent mixing and crystallisation (CMC, Maclennan (2008a)), and acts to systematically reduce mantle-derived geochemical variability as magmas evolve. Previous studies have found CMC to be an important control of geochemical variability on local (Coogan et al., 2000a; Maclennan et al., 2003; Maclennan, 2008a; Gillis et al., 2014) and global scales (Rubin et al., 2009; Shorttle, 2015), in whole-rock (Shorttle et al., 2014) and melt inclusion suites (Neave et al., 2013). Here we explore this model in the context of global patterns of trace element over-enrichment during MORB differentiation (O'Neill and Jenner, 2012). A schematic of the processes that may control trace element over-enrichment, from mantle to crust, is presented in Fig. 2.

This paper is split into six sections, progressing from justifying the choice of model and outlining its behaviour, to comparing it to global MORB and assessing its ability to produce the observed patterns of trace element over-enrichment. We first briefly review evidence for compositionally variable mantle melt supply to the crust and CMC erasing that variability, with local and regional case studies of densely sampled portions of ridge. We then describe the statistical model used for the remainder of the manuscript, which relates CMC to the MgO and trace element structure of differentiated basalt suites. In this model, crystallisation occurs perfectly fractionally (according to equation 1), but diverse primary melts are allowed to have mixed in proportion to their degree of differentiation and relative abundance. We then investigate how key input parameters to the model — the trace element variability of parental melts, their MgO content, and the relative mass of enriched and depleted melts — result in trace element–MgO patterns departing from single melt composition Rayleigh fractionation trajectories. In order to compare the model predictions of trace element over-enrichment to that observed in global MORB, the Gale et al. (2013a) MORB dataset is then used to calibrate the model parameters. We make a direct comparison between model and real gradients of trace element enrichment ($d(\log[C/C_0^1])/d(\mathrm{MgO})$, e.g. Fig. 1), finding CMC to accurately reproduce the relationship between a trace element's over-enrichment and its bulk partitioning behaviour. Finally, we discuss the implications and applicability of our model as a function of melt supply, emphasising that unlike replenishment models it operates independently of steady state axial magma chambers.

The evidence for chemically heterogeneous mantle melts and their mixing during differentiation

A necessary condition for CMC to generate apparent trace element over-enrichment, is for primary magmas entering crustal magma chambers to have a variable trace element composition. The formation of chemically diverse partial melts during decompression mantle melting seems inevitable, even in a chemically homogeneous mantle, given the inferred low porosities at which melting is taking place (Langmuir et al., 1977; McKenzie, 1985; Johnson et al., 1990; Johnson and Dick, 1992). If the prospect of major and trace element heterogeneity in the mantle is considered as well (Allègre and Turcotte, 1986; Hirschmann and Stolper, 1996; O'Nions and Pankhurst, 1974), then the likelihood and amplitude of melt heterogeneity being supplied to the crust becomes even greater. The question then is whether these signals can be effectively transported to shallow mantle and crustal magma chambers, avoiding homogenisation en route.

Petrological work investigating the extraction of mantle melts suggests that they are efficiently focused into dunite channels, thus enabling the disequilibrium transport of melts produced at depth within the melting region (Kelemen et al., 1997). This inference is supported by numerical models exploring reactive channelisation in the mantle, which have found extreme heterogeneity in melts to be preserved during melt focusing into channels (Spiegelman and Kelemen, 2003). Once juxtaposed in magma chambers, these

primary melts will rapidly mix, so it is in primitive basalts and their early forming crystal phases that greatest evidence of melt heterogeneity will be found. Below, data are presented from two densely sampled regions of mid-ocean ridge, which have erupted basalts over a range of MgO and exhibit significant trace element variability. These data demonstrate that where suites of basalts extend to the early stages of magmatic differentiation, the presence of initial chemical variability and its destruction by mixing during crystallisation is an important process in MORB evolution.

The first sample suites we consider are from Iceland (Fig. 3), where previous work has shown CMC to be recorded in both whole rock (Maclennan et al., 2003; Shorttle et al., 2014) and melt inclusion suites (Maclennan, 2008a; Neave et al., 2013). The trace element that we have chosen to track during the differentiation processes is La, which because of its low bulk K_d during mantle melting is likely to exhibit order of magnitude concentration variations in primary melts (e.g. Fig. 2), and La remains incompatible during low pressure fractionation. Fig. 3 (a)–(c) show how the primary chemical variability in basalts/melt inclusions at high MgO/Fo is followed by reduced chemical variability as differentiation proceeds. Data are plotted as $\log[\mathrm{La}/\mathrm{La_{depleted}}]$, where $\mathrm{La_{depleted}}$ is the composition of depleted melts in the given dataset; a normalisation we apply here for consistency with the analysis we will perform subsequently, the appearance of CMC is apparent irrespective of these scalings. In both whole rock and melt inclusion datasets, La varies by 1–2 orders of magnitude in primitive melts, decreasing to ~ 0.5 log units by 5 wt% MgO and $\mathrm{Fo_{80}}$ in the melt inclusions. Below each plot of raw data, the normalised variability profiles (defined as σ/μ, the standard deviation ratioed to the mean) have been calculated in a moving boxcar window centred on each sample (Fig. 3 (d)–(f)). These variability–MgO plots formalise the observation that the maximum variability in La is observed in the most primitive melts and variability subsequently decreases during differentiation.

Although not shown here, the trace element element systematics of Icelandic basalts correlates with their radiogenic isotope and major element composition (Stracke et al., 2003; Maclennan, 2008b; Shorttle and Maclennan, 2011; Shorttle et al., 2013). Therefore, on Iceland there is clear evidence that it is mantle derived variability that is being mixed out during magma chamber processing, and that this mixing must overwhelm (at least at MgO > 5 wt%) any tendency for chemical variability to be created by crustal assimilation or re-injection of mush liquids. As such, fractional crystallisation and mixing of melts with diverse mantle-derived parental compositions are the dominant processes.

The number of data included in Fig. 3 is large, nearly 900 whole rock and 200 melt inclusion analyses. This level of sample coverage is rare on most of Earth's mid-ocean ridge system (e.g. figure 1 of Shorttle (2015)). Having a differentiation series characterised by only a small number of samples makes the higher moments of distributions, such as variance (or worse, variance as a function of MgO), difficult to reliably quantify. In the appendix we demonstrate the sensitivity of trace element differentiation patterns to sample number. In addition to Iceland, however, a submarine portion of the Mid-Atlantic Ridge between 36–38°N, including the FAMOUS segment (Bougault and Heikinian, 1974), has been sampled at high resolution by dredge and submersible. We show a compilation of whole rock and melt inclusion data from this area in Fig. 4 (Gale et al., 2013b; Shimizu, 1998; Laubier et al., 2007, 2012), and as for the Iceland dataset interrogate it for its trace element variability and differentiation trends.

Although there are fewer samples, both whole rock data from the ridge around the FAMOUS region (Fig. 4 (a)) and the whole rock data from the FAMOUS segment itself (Fig. 4 (b)), show evidence of decreasing geochemical variability with decreasing MgO. This pattern is also reproduced in the melt inclusion data from FAMOUS samples (Fig. 4 (c) & (f)); where either taken collectively (white circles), or as the two best characterised samples (ALV519-4-1 in dark purple and ARP73-10-03 in green, n = 31 and 58 respectively), the melt inclusions show decreasing La variability as the forsterite content of their host olivines drop. These observations are consistent with the early work on FAMOUS by Langmuir et al. (1977), who noted the high degree of chemical variability in primitive FAMOUS basalts and took this as evidence for the production and transport of mantle melts of varying chemistry to the crust. We would add to this analysis that, with the most recent sample compilations, there is evidence of this primary magma chemical variability being destroyed by mixing in the crust concurrent with crystallisation.

The appearance of CMC in Iceland and the Famous regions shows a scale invariance. Melt inclusion populations from single eruptions, whole rock suites from a single volcanic zone/segment ($\sim$ 45–90 km of rift), and whole rock from the entire region (200–300 km of rift), all show the same differentiation trajectory of

diminishing variability concurrent with crystallisation. On a larger scale, Rubin and Sinton (2007), Rubin et al. (2009) and Shorttle (2015) have argued for the ubiquity of CMC during magmatic differentiation throughout the global mid-ocean ridge system. Although taking different approaches and using separate datasets, each study finds evidence for significant chemical variability at high MgO, with this variability decreasing concurrent with differentiation. The effect of CMC in global compilations of MORB is also apparent from the analysis of O'Neill and Jenner (2012), where in their figure 2c both the phosphorus and potassium concentrations of basalts with MgO > 8.5 wt% are more variable than at lower MgO. These results point to the general operation of CMC during MORB petrogenesis.

Taken together, the above observations argue for: (1) the supply of diverse melts in terms of their major, trace element, and isotopic composition to MORB magma chambers; and (2) the net effect of differentiation to be a reduction in this primary chemical variability at a given MgO, as magmas mix concurrent with their crystallisation. Magma chamber models that use chromatographic, recharge, or in situ crystallisation to account for incompatible element over-enrichment have not yet attempted to fit these fundamental observations of the nature of MORB magmatism. Our approach however, will be to take these observations as evidence for the importance of CMC in MORB genesis, and for the remainder of the paper investigate CMC's effect on apparent rates of trace element enrichment during differentiation.

Statistical model of concurrent mixing and crystallisation

We use a simple statistical description of CMC to constrain its effect on trace element enrichment during differentiation. The model is based upon that used by Rudge et al. (2013) to mix fractional mantle melts. We leave a full petrological description of CMC for a future study.

A single melt, which has undergone a random amount of concurrent mixing and crystallisation, can be produced in four stages:

1. Define m parental melt compositions entering the system (crust). These melts are the starting compositions that will be fractionated and mixed. (Left hand panel of Fig. 2, $m = 2$.)
2. Generate a random amount of fractionation (top right hand panel of Fig. 2).
3. Generate a random mixture of the parental melt compositions (middle right hand panel of Fig. 2). The key to obtaining behaviour where mixing and crystallisation are concurrent, is to have this degree of mixing increase with the degree of fractionation determined above.
4. The trace element compositions of mixed sources can then be evolved with equation 1, according to the amount of fractionation decided at step 2.

Repeating these steps n times produces a synthetic population of variably differentiated and mixed melts, as in the bottom right hand panel of Fig. 2 (where $n = 300$). We emphasise that in nature we envisage the mixing and crystallisation to be occurring concurrently, and not in the stepwise fashion convenient for calculation. The calculations produce the effect of *concurrent* mixing and crystallisation by having the likelihood of extensive mixing increase with the degree of fractionation. Step 1, the choice of endmember liquid compositions is discussed in subsequent sections. Here, we outline the details of steps 2–4, which relate to the statistical mixing and fractionation model.

The first step of the CMC model is fractional crystallisation. Fractional crystallisation is modelled by generating a uniform deviate lying between 0, no differentiation, and 1, maximum differentiation,

$$\widehat{U} \sim \text{Uniform}(0, 1).$$

The hat on $\widehat{U}$ indicates it that it is a random variable. The remaining liquid mass following crystallisation, X, is then related to $\widehat{U}$ by

$$\widehat{X} = \widehat{X}_{\max}\widehat{U}, \tag{3}$$

where $X_{\max}$ is maximum differentiation reached. In the general case we consider, the endmember parental liquids may not lose the same amount of mass over their differentiation interval. In this case, the derivative

mixed liquid has an $X_{\max}$ produced by linear combination of the $X_{\max}^{(i)}$ from the m endmember parental liquids. the maximum degree of differentiation for the mixed liquid is calculated as

$$\widehat{X}_{\max} = \sum_{i=1}^{m} \hat{r}_i X_{\max}^{(i)}, \tag{4}$$

for $0 \leq X_{\max}^{(i)} < 1$, and where $\hat{r}_i$ is the mass fraction of the ith parental melt in the mixed liquid.

The second stage of the CMC model is to link differentiation, $\widehat{U}$, to mixing, which we do using a mixing parameter $\widehat{N}$. We define the relationship between $\widehat{U}$ and $\widehat{N}$ as

$$\widehat{N} = N_{\min} \left(\frac{N_{\max}}{N_{\min}} \right)^{\widehat{U}^k}, \tag{5}$$

which is an arbitrary choice of functional form, but one which varies the mixing parameter between $N_{\min}$ when $\widehat{U} = 0$ (i.e. an unmixed and un-differentiated melt when $N_{\min} = 1$), and $N_{\max}$ when $\widehat{U} = 1$ (i.e. maximum mixing at maximum differentiation). The parameter k, where $k \geq 0$, is used to control the rate at which mixing occurs as a function of differentiation: the exponent of $N_{\max}/N_{\min}$, $\widehat{U}^k$, is skewed towards 0 as k increases, ensuring that $\widehat{N}$ remains near $N_{\min}$ for longer during the differentiation interval, meaning mixing occurs later. We investigate appropriate choices for k at the end of this section.

Mixing occurs by weighted summation of endmember parental liquids. As differentiation proceeds, the weighted contribution of the m parental liquids to the derivative liquid converges on the proportion in which the parental liquids are present in the system, i.e. more mixing occurs in more differentiated liquids, and their composition is therefore more likely to be that of the system mean. A mixed liquid with initial compositions $\widehat{C}_0$ is generated by randomly mixing between the endmember melt compositions entering the crust,

$$\widehat{C}_0 = \sum_{i=1}^{m} \hat{r}_i C_0^{(i)}. \tag{6}$$

The parameters $(\hat{r}_1, \hat{r}_2, \ldots, \hat{r}_m)$, define the proportions in which the m parental liquids have mixed to produce the derivative liquid. The endmember parental liquids have compositions $C_0^{(i)}$. In all the models presented here we take $m = 2$, i.e. one enriched and one depleted melt composition. The mean system composition before crystallisation, $\overline{C}_0$, is constrained by the endmember melts and the relative mass proportions with which they are present in the system (i.e. entering the crust) ω_i, according to

$$\overline{C}_0 = \sum_{i=1}^{m} \omega_i C_0^{(i)}. \tag{7}$$

Mass conservation requires that the mass fractions of the endmembers obey

$$\omega_i \geq 0, \qquad \sum_{i=1}^{m} \omega_i = 1. \tag{8}$$

Similarly, the weights used in mixing to produce the derivative liquids are such that

$$\hat{r}_i \geq 0, \qquad \sum_{i=1}^{m} \hat{r}_i = 1. \tag{9}$$

To ensure that the random weights produce sample distributions with the appropriate mean composition (equation 7), i.e. $\mathbb{E}(\widehat{C}_0) = \overline{C}_0$, then it is also necessary that

$$\mathbb{E}(\hat{r}_i) = \omega_i. \tag{10}$$

The distribution we use to produce the weights $\hat{r}_i$ is the Dirichlet distribution, details of which can be found in Rudge et al. (2013). The Dirichlet distribution has strong independence properties, which means that the different endmember melts are treated equally according to their relative proportions (ω_i). Formally, the weights are distributed according to a Dirichlet distribution with parameters α_i,

$$\{\hat{r}_1, \hat{r}_2, \ldots, \hat{r}_m\} \sim \text{Dir}(\alpha_1, \alpha_2, \ldots, \alpha_m),$$
$$\alpha_i = (N-1)\omega_i. \tag{11}$$

Dirichlet parameters α_i are chosen such that equation 10 is satisfied. In addition to the mean composition, the mixing parameter N is required to fully define the Dirichlet weights (Rudge et al., 2013). N can range from 1 to ∞, where 1 represents no mixing between parental liquids, and ∞ is complete mixing. The significance of N is illustrated in Fig. 5, where for the scenario $m = 2$ (i.e. the case of two parental melt composition that we study here, one depleted melt, $C_0^{(1)}$, and one enriched, $C_0^{(2)}$) the corresponding distributions of $\widehat{C}_0$ are shown for $N = 1, 2, 16$ & ∞, generating 300 mixed melts in each case. Fig. 5 demonstrates how as N increases the samples converge towards the weighted mean composition of the parental melts ($\mathbb{E}(\widehat{C}_0)$), reducing in chemical variability from a maximum at $N = 1$. Rudge et al. (2013) quantified the relation of the mixing parameter N to the remaining variance in the samples as

$$\text{var}(\widehat{C}_0) \propto \frac{1}{N}. \tag{12}$$

With the relations above, the chemistry of a mixed differentiated liquid can now be calculated using the Rayleigh fractionation equation,
$$\widehat{C} = \widehat{C}_0(1 - \widehat{X})^{(K_d - 1)}. \tag{13}$$

We need to also define the $\widehat{\text{MgO}}$ of the mixed fractionated liquid, as this will be our reference in natural samples for their degree of differentiation. We use a simple linear relation between $\widehat{\text{MgO}}$ and $\widehat{X}$

$$\widehat{\text{MgO}} = \widehat{\text{MgO}}_0 - \frac{(\widehat{\text{MgO}}_0 - \text{MgO}_{\text{min}})}{\widehat{X}_{\text{max}}}\widehat{X}, \tag{14}$$

where $\widehat{\text{MgO}}_0$ is calculated equivalently to $\widehat{C}_0$ using equation 6. Throughout this study we take MgO_{min} as a constant 5 wt%, and we investigate varying $\text{MgO}_0^{(2)}$ between 8–10 wt%. Such a simple relation for a petrologically sensitive major element such as MgO is clearly not accurate in detail, as the pressure of crystallisation and water content will have a large effect on the liquidus phase assemblage and thereby the rate of decrease of MgO as a function of mass loss (Danyushevsky, 2001). We discuss the implications of our choice of $\widehat{\text{MgO}}$–$\widehat{X}$ relationship further in the appendix. However, we emphasise that despite these simplifications, the model captures the essence of a concurrently crystallising and mixing magma system.

Combining the mixing and crystallising steps, and repeating this random generation of melts n times, gives a population of synthetic samples exhibiting CMC behaviour. An illustration of how such as system behaves is given in Fig. 6, according to the prescribed relationship between the mixing parameter, N, and differentiation, X. The top panels, Fig. 6 (a)–(c), show the functional form that N takes over the differentiation interval; from a slow increase in (a), a linear ramp in (b), and rapid mixing from the outset in (c). Note that in all calculations the limits on N are kept constant, with $N_{\text{min}} = 1$ and $N_{\text{max}} = 108$, from equation 12 this translates into a factor of ~ 10 decrease in variance over the differentiation interval, equivalent to the variance reduction seen in Icelandic whole rock suites (Shorttle et al., 2014). Below these panels are the distributions of synthetic samples generated from each of the N–X relations (Fig. 6 (d)–(f)), given the concentration ratio of the two endmember melts ($C_0^2/C_0^1 = 10$), and the proportion of these enriched and depleted melts entering the crust ($\omega_1 = \omega_2 = 0.5$). Fig. 6 (d)–(f) show the strong dependence of the data structure on how N varies as a function of X: where the increase of N is initially slow during differentiation, samples down to ~ 8 wt% MgO retain a record of much of the primary variability entering the system; however, when N increases more rapidly during differentiation melts become mixed at high MgO, until the point where at all MgO they just bracket a simple fractional crystallisation trajectory (Fig.

6 (f)). The collapse in variability during differentiation is measured in Fig. 6 (g)–(i), which show the standard deviation normalised to the mean in a moving boxcar window across the sample sets. In the case of Fig. 6 (i), where almost all primary chemical variability is mixed immediately, the steepening of the data array from fractional crystallisation wins out in controlling the variability–MgO relationship.

It is important to note that for all scenarios in Fig. 6, the composition of the most fractionated melts converges on that of the differentiated equivalent of the mean system composition (dashed black lines). In other words, if mixing is efficient, the limit on enrichment at low MgO in this model is $\widehat{C}_{5\,\mathrm{wt\%}} \approx \overline{C}_{5\,\mathrm{wt\%}} = \overline{C}_0(1 - \overline{X}_{\max})^{(K_d - 1)}$. At this limit, $\widehat{C}_{5\,\mathrm{wt\%}}$ is lower than the equivalently fractionated melt of the pure enriched endmember. But critically for generating the appearance of trace element over-enrichment, $\widehat{C}_{5\,\mathrm{wt\%}}$ is higher than in the differentiated depleted melt. The result is that when mixing is gradual over the differentiation interval, regressions through the samples are steeper than pure fractional crystallisation would predict (compare $d(\log[C/C_0^1])/d(\mathrm{MgO})$ between Fig. 6 (d) and (f)). This is the essential fact that enables the CMC model to predict the appearance of trace element over-enrichment in global MORB.

We have used the relationship between N and variance (equation 12) to map the Icelandic whole rock data from Fig. 3 (a) into an empirical N–MgO relationship (Fig. 6 (a)–(c) blue line). This allows us to pick a style of mixing consistent with natural data. From Fig. 6 (a)–(c) it is apparent that variance changes during CMC are most consistent with a gradual increase in N, and the retention of primary variability over the first few wt% decrease in MgO, as in Fig. 6 (a). This case corresponds to a value for k of 1.2, and is the rate of mixing we use for all subsequent calculations. In detail, N-MgO relationship will vary as a function of crustal architecture and melt supply. However, the correspondence between CMC patterns in Icelandic and Mid-Atlantic whole-rock suites (Figs. 3 and 4), suggests that this choice of N and k captures the systematics of CMC without being overly region specific.

Sensitivity of trace element enrichment trajectories to the style of mixing

Having defined a statistical description of concurrent mixing and crystallisation, we now investigate how key parameters in this model affect the development of trace element over-enrichment during differentiation. Our analysis is focused on the parameters specific to the CMC model we have developed, which we use with two parental melt compositions: C_0^2/C_0^1, the concentration ratio of enriched to depleted melts entering the crust; $\mathrm{MgO}_0^{(1,2)}$, their MgO concentration; and $\omega_{1,2}$, their relative mass fractions in the melts supplied from the mantle. Non-CMC specific model parameters are discussed in the appendices: in the appendix we explore the relationship between MgO and X used in our model and the effective $K_d(\mathrm{MgO})$ this implies; and the appendix also investigates how the distribution of samples across MgO affects the calculated regression parameters. The key result from this section is that within the natural range of the model parameters, parental melt heterogeneity has a large effect on trace element differentiation patterns.

Trace element over-enrichment was defined by O'Neill and Jenner (2012) in the context of gradients in log of trace element versus MgO space (Fig. 1), or $d(\log[C/C_0^1])/d(\mathrm{MgO})$ (where here for convenience we are normalising concentrations to that of the depleted endmember melt C_0^1). We also use this convention, so that plots of real and synthetic samples are presented in $\log_{10}[C/C_0^1]$ versus MgO space (see appendix for a discussion of the implications of this choice). For the synthetic case studies we explore below, a fictive element with $K_d = 0$ is used throughout; when we go on to compare with real data we adopt appropriate mineral specific K_d's. At this stage we also use a single value of $X_{\max} = 0.65$. Applying these constraints, all our model results in this section can be referenced to a limiting gradient of fractional crystallisation for a single liquid composition, which calculated as the mean gradient over the differentiation interval is ~ -0.09. It is the departure from this reference gradient of samples undergoing CMC that is investigated in the following three sections.

Enriched to depleted concentration ratio: C_0^2/C_0^1

In the context of understanding trace element over-enrichment in MORB, the fundamental premise of our CMC model is that melts with diverse trace element composition are entering crustal and shallow mantle magma chambers. The mixing of these melts, concurrent with their evolution by fractional crystallisation,

then enables differentiation trends to depart from the fractional crystallisation path of single liquids. Here we explore the property of the models directly relating to this primary chemical heterogeneity, the concentration ratio between enriched and depleted parental melts, C_0^2/C_0^1.

In Fig. 7 we have varied the ratio C_0^2/C_0^1 between 1 and 1000, and at each step generated 2000 samples from the statistical CMC model from which we can calculate a gradient $d(\log[C/C_0^1])/d(\mathrm{MgO})$. Across this concentration range, the relative proportion of enriched and depleted melts entering the system has been held constant at $\omega_1 = \omega_2 = 0.5$. At one extreme $C_0^2 = C_0^1$, and the differentiation trends of the two liquids, mixed or unmixed, are identical (Fig. 7 (a)). In this case, the samples all lie along the trajectory of pure fractional crystallisation and the regression gradient is ~ -0.09, equal to the fractional crystallisation case. At the opposite extreme $C_0^2/C_0^1 = 1000$, and the net effect of CMC is to produce a sample distribution widely spread over $\log[C/C_0^1]$–MgO space, as the contamination of depleted melts by even small amounts of the enriched endmember dramatically increases their concentration of C (Fig. 7 (c)). Fitting a linear regression to the sample distribution in Fig. 7 (c) (solid black line), now returns a gradient significantly steeper than is attained by pure fractional crystallisation, $d(\log[C/C_0^1])/d(\mathrm{MgO}) = -0.25$. Between the two extreme cases the gradient of trace element enrichment progressively steepens away from the pure fractional case (Fig. 7 (b), solid orange line). Although a trace element enrichment of 1000 between enriched and depleted melts may be at the extreme end of heterogeneity seen in typical mid-ocean ridge basalts (e.g. Sobolev (1996) find a maximum enrichment in La of ~ 270 between their most enriched and ultra-depleted inclusions), Fig. 7 (b) shows that there is resolvable steepening of the trace element enrichment gradient for any $C_0^2/C_0^1 \geq 2$.

The corresponding variability–MgO profiles for the values of C_0^2/C_0^1 investigated are given in the bottom panels of Fig. 7. Across this range variability goes from nearly constant as a function of MgO (Fig. 7 (d)), to showing a strong negative correlation with degree of differentiation (Fig. 7 (f)). In Fig. 7 (e) we quantify the mixing behaviour during differentiation across all C_0^2/C_0^1 by calculating the average gradient $d(\sigma/\omega)/d(\mathrm{MgO})$, which we term the mixing gradient, from profiles equivalent to those shown in Fig. 7 (d) & (f). The mixing gradient, plotted in orange (Fig. 7 (e)), is positive for values of $C_0^2/C_0^1 > 1.4$, which defines the threshold at which CMC type behaviour becomes apparent (gradients, $d(\log[C/C_0^1])/d(\mathrm{MgO})$, deviating from -0.09). The mixing gradient increases until $C_0^2/C_0^1 \sim 10$, after which point it plateaus. Over most of this range CMC is clearly resolvable in the synthetic data.

The key point from the above model results is that the appearance of mixing behaviour in sample sets varies strongly according to the trace element heterogeneity of the parental melts. This is true both in terms of the gradient in trace element–MgO space, and for the development of a resolvable decrease in geochemical variability during differentiation. As we will go onto show, natural MORB endmember melt compositions lie in the range $0.5 < \mathrm{C}_0^2/\mathrm{C}_0^1 < 20$ depending upon the trace element considered, and thus will span a wide variety of the behaviour seen in Fig. 7. From this simple analysis it is therefore evident that those elements showing the greatest chemical variability in primary melts, will show the greatest departure from simple fractional crystallisation trends.

MgO content of parental melts: $\mathrm{MgO}_0^{(1,2)}$

Analogous to trace element heterogeneity in the parental MORB melts is the possibility that the extreme trace element enriched and depleted melts may also vary in their MgO content. We discuss the evidence for and potential causes of an MgO offset between enriched and depleted parental melts. Here, we focus in general on the effect a variable $\mathrm{MgO}_0^{(1,2)}$ would have for trace element over-enrichment during CMC.

Fig. 8 shows the result of varying the MgO content of the enriched endmember melt ($\mathrm{MgO}_0^{(2)}$) from 10 to 8 wt%. Over this range we have used a constant $X_{\max} = 0.65$, held $C_0^2/C_0^1 = 10$, and the enriched melt fraction at $\omega_2 = 0.5$. Note that when we apply the CMC model to natural data, equation 4 is used to appropriately scale $X_{\max}$; leaving $X_{\max}$ constant here means that the results of Fig. 8 are an upper bound on the trace element enrichment for a given $\mathrm{MgO}_0^{(2)}$ change. In reducing $\mathrm{MgO}_0^{(2)}$ from 10 to 8 wt% Fig. 8 (b) shows that $d(\log[C/C_0^1])/d(\mathrm{MgO})$ steepens by ~ 0.06. This effect results from the enriched and depleted melts now mixing to simultaneously increase the depleted melts' trace element concentration and lower their MgO, creating the appearance of fractionation via mixing.

The lower panels of Fig. 8 record how trace element variability evolves in the synthetic datasets during CMC. Tracked by the mixing gradient, $d(\sigma/\omega)/d(\mathrm{MgO})$, we see that the mixing out of primary variability is not significantly affected over the MgO range investigated (Fig. 8 (e)). The primary affect of lowering $\mathrm{MgO}_0^{(2)}$ is to create an early interval during differentiation where geochemical variability is low, because melts in this region primarily sample the depleted endmember (Fig. 8 (f)). There is a suggestion that such a phenomenon may be occurring in natural datasets: the Icelandic whole rock data presented in Fig. 3 (a) and melt inclusions from the Borgarhraun eruption (Maclennan et al. (2003); Maclennan (2008a), reproduced in Fig. 3 (c)), both record a decrease in variability in the most primitive melts (high MgO or host olivine Fo), which in the case of the Borgarhraun melt inclusions clearly corresponds to the melts becoming more depleted.

These results demonstrate that variation in parental melt MgO is an important, though non-essential, parameter for modelling trace element trends during differentiation: whilst having $\mathrm{MgO}_0^{(2)} < \mathrm{MgO}_0^{(1)}$ steepens gradients of trace element enrichment, it cannot create a deviation from simple fractional crystallisation behaviour where the incoming melts are homogeneous (Fig. 8 (a)). When there is trace element variability however, also considering $\mathrm{MgO}_0^{(1,2)}$ heterogeneity can double the offset between the observed rate of trace element enrichment and that predicted by fractional crystallisation.

Mass fraction of enriched melts: ω_2

The final parameter that we show differentiation trends to be sensitive to is the mass fraction of enriched melts involved in mixing, ω_2. In considering just two mixing endmember melts, our modelling of CMC is a simplification of the natural scenario where a continuum of diverse melt compositions may be produced over the melting interval and supplied to magma chambers (e.g. Fig. 2). In this sense our reduction of the model to two compositions can be viewed as exploring mixing between average enriched and depleted melts. There is some support for this kind of simplification being a more appropriate model for natural systems than the endmember case of pure fractional melting: Rudge et al. (2013) found that joint trace element–isotope systematics in Icelandic basalts were best explained by a deep homogenisation interval within the melt column, which produced an average enriched melt that mixed with melts of the depleted peridotite matrix to produce pseudo-binary chemical arrays.

In Fig. 9 we have investigated the effect of varying ω_2 between 0 and 1 on gradients of trace element enrichment ($d(\log[C/C_0^1])/d(\mathrm{MgO})$) and mixing gradients ($d(\sigma/\omega)/d(\mathrm{MgO})$). Fig. 9 (b) shows that at either extreme, where $\omega_2 = 0$, or 1, the gradient of trace element enrichment falls back onto that expected for pure fractional crystallisation. This is because the system reduces to having just a single melt composition. At intermediate ω_2 trace element enrichment gradients become over-steepened when compared to the fractional crystallisation case, by up to ~ 0.05. The maximum effect on the enrichment gradients is reached at $\omega_2 \approx 0.3$, although this depends on the choice of C_0^2/C_0^1 (here held at 10). An important feature of Fig. 9 (b) is that over a broad range, from $\omega_2 = 0.2$–0.4, the gradient of trace element enrichment is nearly constant. Therefore, if natural values of ω_2 fall in the range 20–40%, then our comparison of the CMC model to natural MORB will not be sensitive to the exact choice of ω_2.

The effect of varying ω_2 on gradients of trace element mixing, Fig. 9 (e), is more asymmetric, as trace element enriched melts tends to dominate the variance. Therefore, even with very small mass fractions of the enriched melt present in the mixture, CMC-like trends of reducing variability with MgO are apparent (Fig. 9 (d)). Conversely, when the enriched melt fraction is large, small amounts of depleted melt are unable to generate significant variability (Fig. 9 (f)).

These results show that when present, enriched melts have a strong effect on the gradient of trace element enrichment, and the appearance trace element variability, during differentiation. By varying ω_2, the magnitude of trace element over-enrichment from CMC can be up to half that seen in natural datasets (Fig. 1). The response of the trace element enrichment gradient to ω_2 is non-linear, with a strong effect seen for even relatively modest contributions of enriched melt to the mixture ($> 5\%$). This suggests natural systems, with heterogeneous melt supply, will be very susceptible to CMC modifying trace element enrichment gradients during differentiation.

10

Identifying mixing model parameters from natural data

In the previous section we demonstrated that rates of trace element enrichment during differentiation are sensitive to the trace element concentration of endmember melts going into the mixture (C_0^1/C_0^2), the MgO content of endmember melts ($\mathrm{MgO}_0^{(1,2)}$), and the relative mass fraction of enriched melts (ω_2). To understand whether CMC can explain the trace element over-enrichment seen in natural MORB datasets (Fig. 1), we next need to constrain the appropriate values for each of these parameters. We identify these constraints in the context of our simplification that CMC can be approximated by mixing between two endmember melt compositions. In this section we step through the natural observations that enable us to make these estimates, starting with the MgO content of the endmember melts, which will be a useful parameter when characterising C_0^1/C_0^2.

MgO of primitive depleted and enriched MORB: $\mathrm{MgO}_0^{(1,2)}$

We have taken two approaches to estimating MgO contents of primitive enriched and depleted melts. In the first we use an index of enrichment and plot this against MgO, looking to see whether there is a slope on the high-MgO side of this distribution: i.e. whether there is evidence for the most primitive enriched melts existing at a lower MgO than primitive depleted melts. We have performed this analysis in Fig. 10 (a), where we have taken our index of enrichment to be the trace element ratio La/Yb. The raw La/Yb has been geographically normalised, subtracting the local mean and dividing by the local standard deviation, to produce a dataset that normalises out local differences in mean degree of enrichment (Shorttle, 2015). The grey points in Fig. 10 (a) are the MORB data from Gale et al. (2013a), and the black lines are percentile estimates of where the high-MgO side of the data distribution lies at a given La/Yb. Whether the high-MgO side of the data is described by the 50th or 99th percentile, in each case there is a trend towards the most enriched compositions having lower MgO. We repeat this analysis in Fig. 10 (b) using a range of trace element ratios, still geographically normalised, and all the high-MgO percentiles trend towards lower MgO as the data become more enriched. To demonstrate that this result is not an artefact of the normalisation procedure we also present the high-MgO percentiles for the data without geographical normalisation in Fig. 10 (c), which still show that as samples become more enriched their highest MgO drops. The magnitude of this decrease is between 1 and 2 wt% MgO (Fig. 10 (b) & (c)).

The second approach we take is to look at the bulk distribution of MORB samples, split between those classified as enriched-MORB (E-MORB) and all other basalts (N-MORB), and evaluate whether there is any offset between their MgO distributions. We carry out this analysis in Fig. 10 (d) & (f), for definitions of E-MORB based on La/Sm and K/Ti thresholds respectively (Gale et al., 2013a; Smith et al., 2001). Using either incompatible element ratio to split up the MORB dataset, it is apparent from Fig. 10 (d) & (f) that enriched basalts on average lie to lower MgO than depleted basalts. Applying Mann-Whitney or student's t-tests to these MgO distributions confirms that the enriched basalts have lower MgO than depleted basalts with $> 95\%$ confidence. The difference in mean MgO between the two distributions is ~ 0.25 wt%.

The analysis of the distributions of E-MORB and N-MORB confirms the result arrived at by calculating the high-MgO percentiles. However, it is less useful for characterising the endmember melt MgO contents needed for the CMC model as it includes a majority of differentiated basalts. For defining $\mathrm{MgO}_0^{(1)}$ and $\mathrm{MgO}_0^{(2)}$ we instead use Fig. 10 (b), which includes an attempt to normalise out spatial biases in the data distribution. The vertical grey lines in Fig. 10 (b) mark the ends of the 95th percentile high-MgO slope, indicating that for the depleted endmember $\mathrm{MgO}_0^{(1)} \approx 9.5$ wt%, and for the enriched endmember $\mathrm{MgO}_0^{(2)} \approx 8.5$ wt%. These are the values we use in modelling the natural dataset; compared to the same result implied from the raw data (Fig. 10), an MgO difference of 1 wt% between enriched and depleted appears conservative.

Before moving on, it is useful to consider how an MgO difference between depleted and enriched melts may have arisen, as plausible mechanisms for such a phenomenon may help support the observation.

Polybaric fractional fusion of homogeneous peridotite will on its own produce primary melts varying in their MgO. However, in this case the relationship between MgO and enrichment will be inconsistent with enriched melts having lower MgO: high pressure, low-degree, melts will have higher MgO than low pressure

depleted melts (also see the appendix). Instead, we consider three viable mechanisms for forming lower MgO enriched compared with depleted MORB:

1. If the mantle contains pyroxenite or eclogitic lithologies, especially those with a silica excess, melts with extremely low MgO can form (Lambart et al., 2013). Even if these melts initially react with surrounding peridotite, melting of the hybridised lithology may itself produce low MgO melts.

2. Based on their incompatible trace element budget enriched melts are also likely to be proportionally wetter than dry melts (Michael, 1995). Melts with higher water contents will have depressed plagioclase saturation temperatures, extending their olivine only differentiation interval (e.g. Danyushevsky (2001) and the appendix). The heat evolved during differentiation increases for multi-phase saturation (Ghiorso, 1997). Wet melts will therefore initially buffer their cooling less than dry melts, and so for a given rate of heat loss more quickly evolve to low MgO (see the appendix).

In either of these cases, melts with high concentrations of incompatible trace elements may also be expected to have lower MgO.

The trace element composition of endmember melts: C_0^2/C_0^1

The trace element diversity of primary melts is key for CMC being able generate trends of trace element enrichment deviating from simple fractional crystallisation. In this section we quantify the trace element diversity present in primitive MORB for 18 trace elements spanning a range of incompatibility from Th–Y.

Fig. 11 (a) plots the log-normal variability of trace elements in basalts with ≥ 8.5 wt% MgO (i.e. in the range where melts may be parental). With the elements ordered in Fig. 11 (a) by increasing incompatibility from left-to-right, it is clear that the most incompatible trace elements exhibit the greatest variability. This observation matches what has been found previously in MORB whole rock (Schiano et al., 1993), and melt inclusion datasets (Sobolev, 1996; Laubier et al., 2012). The order of variability seen between the elements in Fig. 11 (a) is consistent with an origin from fractional melting of the mantle controlled by bulk K_d (Schiano et al., 1993), followed by the transport of these diverse melts to shallow mantle and crustal magma chambers (Spiegelman and Kelemen, 2003). The high variability of incompatible trace element concentration in primitive MORB means that their differentiation trends will depart significantly from simple fractional crystallisation during CMC (e.g. Fig. 7).

In Fig. 11 (b) we estimate C_0^2/C_0^1 using the same suite of primitive MORB. C_0^2/C_0^1 is calculated by averaging the trace element composition of the most enriched 20/10/5% of MORB, and dividing this by the trace element composition of the most depleted 20/10/5% of MORB. We use La/Yb as the index of enrichment for the purposes of this filtering, although other incompatible trace element ratios provide similar results. The C_0^2/C_0^1 curve we use in subsequent modelling is that defined by the upper and lower 10% of MORB (Fig. 11 (b), line with points), the structure of which is very similar to the raw variability in the elements (Fig. 11 (a)).

Estimating fraction of enriched melt in MORB: ω_2

Having characterised both the trace element and MgO content of primitive MORB, the final important parameter for magma mixing is the relative proportion of enriched and depleted melts. As for trace element diversity, we emphasise that a heterogeneous source is not a requirement for having a finite mass of enriched melts reaching MORB magma chambers: fractional melting alone will generate a trace element enriched population of melts. The approaches we consider for estimating ω_2 are:

1. Mass balancing between the average crustal composition and the enriched and depleted parental melt endmembers, which were calculated in the previous section.

2. Forward modelling mantle melting to predict the relative mass production of enriched and depleted melts.

We explore each below.

The results of mass balancing between parental melt compositions and mean crust are shown in Fig. 11 (b). The analysis is restricted to the most incompatible elements, because with increasing compatibility the

distinction between enriched and depleted melts diminishes, which lessens the constraint that mass balance offers. The fraction of enriched melt implied by mass balance varies from 22% to 44%, with a mean of 33%. An ω_2 of 33% will produce enrichment gradients distinct from those produced by fractional crystallisation (Fig. 9). It is also within the window of ω_2 values spanning $\sim$ 20–40%, where ω_2's effect on enrichment gradients is nearly constant (Fig. 9 (b)). Therefore, the 22% range in values of ω_2 given in Fig. 11 (b), will not translate to significant changes in modelled enrichment gradients.

We next constrain likely values of ω_2 with a modelling approach, considering both the possibility that the enriched melts are supplied from homogeneous lherzolite melting, and/or from lithological heterogeneities. The ω_2 calculated this way represents the average fractional flux of enriched melts from a melting region. Of course, any single suite of basalts could derive from parental melts more or less weighted to enriched compositions than this.

In Fig. 12 we calculate the mass fraction of enriched melts supplied to the crust, aggregating over a 2D melting region (Shorttle et al., 2014). Fig. 12 (a) & (b) show the case for a fixed mass fraction of pyroxenite in the source (X_{px} = 5%, Hirschmann and Stolper (1996), of either G2 (Pertermann and Hirschmann, 2003) or KG1 (Kogiso et al., 1998)), and vary the mantle potential temperature between 1260 and 1390°C. We separate out the scenarios where melts are only aggregated from a pyroxenite lithology (Fig. 12 (a)), and where the pyroxenite melts are summed with the first 5% melting from lherzolite (its 'low degree' melts, Fig. 12 (b), similar to Rudge et al. (2013)). For either pyroxenite composition modelled, and across the range of potential temperatures, the pyroxenite derived melt fraction is 12–45%, or including the contribution from low degree lherzolite melts, up to 55%. Comparing these values of ω_2 to the sensitivity analysis performed in Fig. 9, indicates that for all cases the mass of enriched melt is enough to have a significant effect on gradients of trace element enrichment.

We also explore a range of pyroxenite source mass fractions at constant mantle potential temperature (1330°C, chosen to produce $\sim$ 7 km of crust for pure lherzolite). The key result from this analysis is Fig. 12 (d), which shows that without pyroxenite present the mass of low degree lherzolite melts is $\sim$ 6%. Therefore, even in the absence of lithological heterogeneity, fractional melting of lherzolite will exert some leverage on the gradients of trace element enrichment by CMC processes. Even small amounts of lithological heterogeneity compound this contribution from low degree lherzolite melts, such that enriched melts quickly dominate the incompatible element budget of the crust (Pertermann and Hirschmann, 2003).

The above analysis indicates that constraints on ω_2 from mass balance and modelling are in agreement: sources containing 5–10% pyroxenite fraction, melting between 1300–1350°C, can produce the 33% enriched melt fraction inferred by mass balance. In subsequent modelling ω_2 is therefore taken as 33%, which corresponds to a 5% source mass fraction of MORB-like pyroxenite (G2, Pertermann and Hirschmann (2003)), melting with a potential temperature of 1330°C, and producing $\sim$ 7 km of crust. These inferred parameters for the MORB source are consistent with the previous estimate from Hirschmann and Stolper (1996).

Applying CMC to understand trace element enrichment during differentiation in global MORB

We next take the constraints on the CMC parameters from the previous section and address the question presented in Fig. 1, of whether CMC can produce the observed trends over trace element over-enrichment in MORB.

The CMC model is now additionally run with realistic partition coefficients (Table 1, assuming a crystallising assemblage ol_{18} : $plag_{42}$: cpx_{40} from O'Neill and Jenner (2012)) and using equation 4 to modify the maximum degree of differentiation ($\widehat{X}_{max}$) according to the enriched:depleted melt proportions in any given sample. The raw results of running the CMC model using these constraints are presented in Fig. 13, where the MORB data from Gale et al. (2013a) for three trace elements in grey are overlain by an equal number of samples generated by the CMC of an enriched and depleted melt. The synthetic datasets bear a close resemblance to the natural data, with the gradient of trace element enrichment steepening as the element considered becomes more incompatible from Yb–La. The close overlap between the synthetic data and natural data indicates the efficacy of our selection of endmember compositions, C_0^1 and C_0^2. The trajectory

of trace element variability during mixing (bottom panels of Fig. 13) is complicated in a global dataset because of regional differences in mean enrichment and variability (Shorttle, 2015). However, both the model and natural data show a transition where the mixing gradient steepens from compatible to incompatible elements.

Fig. 13 (b) and (c) also show that the shape of the data distribution is similar between natural and synthetic datasets. In particular, considering just the most enriched natural MORB at a given MgO, there the slope of enrichment is less than predicted for pure fractional crystallisation, whereas the depleted side of the MORB distribution shows much greater enrichment during differentiation than either fractional crystallisation or the mean for the whole dataset. These observations support a corollary of a pure CMC model: that mixing can only make the most enriched parental MORB less enriched than would be predicted by their pure fractional crystallisation alone. Conversely, mixing can only make the most depleted MORB more enriched than pure fractional crystallisation. The net effect of this is that the upper limit to the global MORB distribution is nearly horizontal, whereas the lower limit sharply rises towards a more enriched mean composition.

The relevant parameter for characterising trace element behaviour during differentiation is the gradient of enrichment, $d(\log[C/C_0^1])/d(\mathrm{MgO})$, which in Fig. 14 (a) we plot for 18 trace elements as a function of their C_0^2/C_0^1 (black line). We also plot the gradients obtained from natural MORB as open circles (Gale et al., 2013a). Fig. 14 (a) shows that modelling the mixing of primary heterogeneity concurrent with fractionation provides an accurate fit to trace element enrichment gradients seen in natural MORB. To a first order, CMC is also able to reproduce the trend of the natural data when enriched and depleted parental melts are given the same MgO (grey line). We can also compare the intercepts of the regressions at 10 wt% MgO between MORB and the CMC model (O'Neill and Jenner, 2012). Fig. 14 (b) shows the results for the intercepts, again for the case where $\mathrm{MgO}_0^{(2)} < \mathrm{MgO}_0^{(1)}$ (black line) and $\mathrm{MgO}_0^{(2)} = \mathrm{MgO}_0^{(1)}$ (grey line). Models run with both parental MgO conditions capture the essential feature of MORB: that the intercept increases as a function of trace element variability, or C_0^2/C_0^1.

In Fig. 14 (c) & (d) we investigate how varying the fraction of enriched melts used in the model, ω_2, affects the gradients and intercepts. As suggested by Fig. 9, the gradient of trace element enrichment can be matched by a wide range of ω_2 (Fig. 14 (c)). The position of the intercept however, is more sensitive to the mean enrichment of the system (Fig. 14 (c)): as the system becomes on average more enriched the whole data array is shifted upwards in proportion to C_0^2/C_0^1, increasing the intercept. The observed intercepts for MORB are best matched by a model with between 30–50% enriched melt.

A more formal comparison between models of MORB differentiation is shown in Fig. 15, where the modelled gradients are plotted against observed gradients. In addition to CMC, we here consider two reference models: (1) simple fractional crystallisation of a homogeneous parental melt composition (i.e. equation 1); and (2) a model where there is primary chemical variability (i.e. $C_0^2 \neq C_0^1$, and using the values from Fig. 11), but where mixing occurs randomly and independently of the degree of differentiation. Fig. 15 (a) shows that neither pure fractional crystallisation of a single melt composition, nor fractionation of variable melt compositions with mixing occurring independently of the degree of differentiation, can produce sufficiently steep trace element enrichment gradients to match the natural data. Allowing $\mathrm{MgO}_0^{(2)} < \mathrm{MgO}_0^{(1)}$ and mixing independent of differentiation does produce steeper gradients than simple fractional crystallisation (dark green triangles, Fig. 15 (a)). However, it is the CMC models, which relate the amount of mixing to the degree of differentiation, that produce the best fits (black and grey symbols). A comparison between modelled and observed intercepts is also shown (Fig. 15 (b)). Fractional crystallisation provides a poor fit to the natural data, showing a large scatter around the observed intercepts. CMC modelled with a difference in $\mathrm{MgO}_0^{(1,2)}$ again performs best, showing a close match for all elements considered.

A quantification of the fits between each of the models tested in Fig. 15 and global MORB can be found in Table 2. These results show that models allowing mixing concurrent with fractionation consistently provide the best fit to the trends of trace element enrichment in natural MORB. We stress that the goodness of fit CMC achieves to natural data was found without inversion to find optimal model parameters: appropriate model parameters were selected from analysis of natural MORB and modelling independently of goodness of fit in Fig. 15.

Discussion

The results from the previous sections show the sensitivity of MORB differentiation trends to heterogeneity in the primary melts being supplied to magma chambers. In particular, given realistic choices of primary magmatic chemical diversity and the relative fraction of enriched melt, concurrent mixing and crystallisation is able to accurately reproduce the trends of trace element enrichment in global MORB. For models that seek to use trace element over-enrichment as evidence for more complex magma chamber processes, we view CMC as a null hypothesis: mantle melting will almost inevitably produce a diverse range of melt compositions and these will be transported to low pressure where they can cool, crystallise, and mix. Additional magma chamber processes capable of generating trends of trace element over-enrichment must be acting on top of this initial condition, which already predisposes the system to produce such trends. In this section we discuss in what settings CMC may be the dominant mechanism of generating trace element over-enrichment, and to what extent deviations from simple fractional crystallisation behaviour mask information about mantle composition.

Applicability of MORB evolution models as a function of melt supply

The models recently proposed to explain trace element over-enrichment in MORB develop steady state magma chambers, where repeated generations of melt supply (from the mantle and/or mush), melt extraction, and crystallisation are capable of driving basalts to more enriched compositions than expected by simple fractional crystallisation (O'Neill and Jenner, 2012). Steady state magma chambers are likely to only exist at intermediate–fast spreading rates, where the melt flux to the ridge axis is sufficient to sustain a permanent magma reservoir (Sinton and Detrick, 1992). Below this threshold melt flux (or spreading rate), crustal magma chambers may form transiently in response to new batches of melt being supplied from the mantle. In this case, the steady state processes required in the O'Neill and Jenner (2012) and Coogan and O'Hara (2015) models may not be able to operate to generate trace element over-enrichment trends. Therefore, if these models of magma chamber processes are the only means of generating trace element over-enrichment, we might expect the global MORB dataset to show a steepening of enrichment gradients as a function of spreading rate.

We have tested the hypothesis that melt supply influences trace element over-enrichment in Fig. 16. The Gale et al. (2013a) dataset has been split into spreading rate bins of width 30 mm/yr, for three incompatible trace elements that have abundant analyses and show the strongest over-enrichment (La, Ce and Nd). We consider both the whole MORB dataset (Fig. 16 (a) & (b)), and that from plume-free portions of ridge (Fig. 16 (c) & (d)), as changes in melt flux due to mantle potential temperature could affect the results (see also the appendix). If melt supply affected the trace element over-enrichment process, we would expect to see a steepening of the calculated gradients from low to high spreading rate in Fig. 16. However, we observe no correlation between trace element enrichment and spreading rate, despite the range of spreading rates investigated implying an order of magnitude change in melt flux.

The presence of trace element over-enrichment in suites of MORB across all spreading rates, suggests that a process independent of the requirement for steady state magma chambers must be operating. We suggest that this process is the concurrent mixing and crystallisation of heterogeneous mantle melts, which will be supplied from a decompressing partially melting mantle irrespective of spreading rate. At higher melt fluxes, processes such as those described by O'Neill and Jenner (2012) and Coogan and O'Hara (2015) may operate on top of primary mantle-derived chemical diversity to produce trace element over-enrichment trends.

How does CMC preserve or destroy information on parental melts and mantle sources?

It was emphasised by Coogan and O'Hara (2015) that magma chamber processes involving recharge, mixing, tapping and crystallisation will obscure mantle-derived chemical signals. In particular, they suggested that trace element ratios such as Sm/Nd may be fractionated away from their mantle value, compromising our interpretation of the Nd isotopic evolution of the mantle. Given this insight, it is useful to consider the implications of CMC for interpreting mantle geochemistry.

Our proposal that CMC describes MORB evolution agrees with the Coogan and O'Hara (2015) analysis in an important respect: CMC by definition achieves the destruction of mantle derived variability during differentiation. Therefore, CMC has to mean that less information on the chemical structure of the mantle will be preserved, compared to a scenario where melts undergo isolated evolution prior to eruption. However, CMC predicts less severe consequences for our characterisation of mantle compositional structure than the Coogan and O'Hara (2015) and O'Neill and Jenner (2012) models. Provided we can obtain enough samples to characterise the mixing and differentiation process (see also the appendix), then in CMC the mean path followed during differentiation is that of the weighted mean of melts entering the crust. As such, differentiated mixed basalts represent a convenient natural average of melts supplied to the crust, which with simple reverse fractional crystallisation can be restored to a composition reflecting that of average primitive melts. This conclusion supports the large body of work that has inferred mantle physical and chemical properties from fractionation corrected datasets and their relationship to geophysical properties of the ridge, exemplified by Na_8–ridge depth correlations (Klein and Langmuir, 1987; Langmuir et al., 1992; Gale et al., 2013a; Dalton et al., 2014; Gale et al., 2014).

More fundamentally, we have seen that in CMC it is the concentration ratio of enriched to depleted melts that is critical for generating trace element over-enrichment during differentiation. This primary diversity of mantle melts is a direct consequence of the fractional nature of mantle melting, the efficiency of diverse melt transport out of the mantle, and the presence of trace element and lithological mantle heterogeneity. In this respect, the deviation of trace element differentiation trends from simple fractional crystallisation can be viewed as a sensitive indicator of mantle sources and melting processes. Therefore, despite mixing and crystallisation, or in some respects because of it, the trace element systematics of MORB may still contain much information on mantle chemical structure and the physics of melting.

Conclusions

We have used a simple statistical model of concurrent mixing and crystallisation (CMC) to couple the evolution of trace element concentration, variability, and MgO in suites of basalts. Key parameters going into the model are: the rate of mixing during differentiation; the difference in trace element concentration between enriched and depleted melts; the primitive MgO of enriched and depleted melts; and the relative proportion of enriched and depleted melts. Adjusting these parameters results in differentiated suites of basalt that have markedly different gradients in trace element–MgO space. Importantly, we find that when there is primary variability in the trace element composition of melts entering the crust, CMC will produce gradients of trace element enrichment steeper than those possible from fractional crystallisation alone (i.e. $d(\log[C])/d(\text{MgO}) < -0.1$).

As a test of the CMC model we applied it to a compilation of global MORB, to assess whether CMC can produce the observed pattern of the most incompatible elements showing the strongest trends of over-enrichment. We first used the MORB dataset to define appropriate input parameters for the model: the enriched to depleted concentration ratio (C_0^2/C_0^1) for a range of trace elements in primitive melts was identified; heterogeneity in the MgO of primitive enriched and depleted melts was evaluated, with there being some evidence that primitive enriched melts have up to 1 wt% lower MgO than primitive depleted melts; and modelling of lithologically homogeneous and heterogeneous mantle melting was performed, showing that the proportion of trace element enriched melt entering the crust may range from 10–40%. Within these constraints the CMC model was able to accurately reproduce the structure of trace element enrichment in global MORB. Comparison of the natural data to alternative model cases, where primary heterogeneity in melt composition is present, but mixing is not permitted, showed that mixing and crystallisation happening *concurrently* is a key requirement for the systematics of MORB to be reproduced.

Our analysis of the global MORB dataset for a dependence of the degree of trace element over-enrichment on melt supply (for which spreading rate was taken as a proxy), showed no correlation between the two. This result implies that in addition to the steady-state magma chamber processes that have been proposed to generate trace element over-enrichment, another process must be present that is not sensitive to melt supply. We suggest this process is CMC, a direct consequence of diverse primary mantle melts being transported to crustal magma lenses, followed by their mixing and crystallisation.

16

Magma-chamber based models have emphasised the potential difficulty of relating trace element variability in basalt suites to mantle source and process, due to the ability of those models to generate large departure from simple reversible fractionation trends. The CMC model presented here is partly in agreement with that prediction: information on primary mantle variability is undoubtedly lost during low pressure magma mixing. However, the nature of CMC means that the way in which information loss translates into gradients in trace element–MgO space is intimately linked to mantle processes; specifically the ability to form and preserve diverse melt chemistries during mantle melting and segregation. Therefore, the major and trace element characteristics of differentiated suites of basalts may still preserve important information about mantle processes, even when mixing has occurred.

Acknowledgements

References

Albarède, F., 1985. Regime and trace-element evolution of open magma chambers. Nature 318, 356–358.

Allègre, C.J., Turcotte, D.L., 1986. Implications of a two–component marble–cake mantle. Nature 323, 123–127.

Asimow, P.D., Dixon, J.E., Langmuir, C.H., 2004. A hydrous melting and fractionation model for mid-ocean ridge basalts: application to the Mid-Atlantic Ridge near the Azores. Geochemistry, Geophysics, Geosystems 5.

Asimow, P.D., Ghiorso, M.S., 1998. Algorithmic modifications extending MELTS to calculate subsolidus phase relations. American Mineralogist 83, 1127–1131.

Bougault, H., Heikinian, R., 1974. Rift valley in the Atlantic Ocean near 36°50ń: petrology and geochemistry of basaltic rocks. Earth and Planetary Science Letters 24, 249–261.

Bowen, N.L., 1915. The later stages of evolution of the igneous rocks. The Journal of Geology 121, 1–91.

Breddam, K., 2002. Kistufell: Primitive melt from the Iceland mantle plume. Journal of Petrology 43, 345–373.

Breddam, K., Kurz, M.D., Storey, M., 2000. Mapping out the conduit of the Iceland mantle plume with helium isotopes. Earth and Planetary Science Letters 176, 45–55.

Bryan, W.B., Thompson, G., Frey, F.A., Dickey, J.S., 1976. Inferred geologic settings and differentiation in basalts from the Deep-Sea Drilling Project. Journal of Geophysical Research 81, 4285–4304.

Chauvel, C., Hémond, C., 2000. Melting of a complete section of recycled oceanic crust: Trace element and Pb isotopic evidence from Iceland. Geochemistry, Geophysics, Geosystems 1.

Coogan, L.A., Kempton, P.D., Saunders, A.D., Norry, M.J., 2000a. Melt aggregation within the crust beneath the Mid-Atlantic-Ridge: evidence from plagioclase and clinopyroxene major and trace element compositions. Earth and Planetary Science Letters 176, 245–257.

Coogan, L.A., O'Hara, M.J., 2015. MORB differentiation: *in situ* crystallisation in replenished-tapped magma chambers. Geochimica et Cosmochimica Acta 158, 147–161.

Coogan, L.A., Saunders, A.D., Kempton, P.D., Norry, M.J., 2000b. Evidence from oceanic gabbros for porous melt migration within a crystal mush beneath the Mid-Atlantic-Ridge. Geochemistry, Geophysics, Geosystems 1.

Dalton, C.A., Langmuir, C.H., Gale, A., 2014. Geophysical and geochemical evidence for deep temperature variations beneath mid-ocean ridges. Science 344, 80–83.

Danyushevsky, L.V., 2001. The effect of small amounts of H_2O on crystallisation of mid-ocean ridge and backarc basin magmas. Journal of Volcanology and Geothermal Research 110, 265–280.

Danyushevsky, L.V., Plechov, P., 2011. Petrolog3: integrated software for modeling crystallization processes. Geochemistry Geophysics Geosystems 12.

Eason, D.E., Sinton, J.M., 2009. Lava shields and fissure eruptions of the Western Volcanic Zone, Iceland: Evidence for magma chambers and crustal interaction. Journal of Volcanology and Geothermal Research 186, 331–348.

Elderfield, H., Schultz, A., 1986. Mid-ocean ridge hydrothermal fluxes and the chemical composition of the ocean. Annual Reviews in Earth and Planetary Sciences 24, 191–224.

Gale, A., Dalton, C.A., Langmuir, C.H., Su, Y., Schilling, J.G., 2013a. The mean composition of ocean ridge basalts. Geochemistry, Geophysics, Geosystems 14.

Gale, A., Langmuir, C.H., Dalton, C.A., 2014. The global systematics of ocean ridge basalts and their origin. Journal of Petrology 55, 1051–1082.

Gale, A., Laubier, M., Escrig, S., Langmuir, C.H., 2013b. Constraints on the melting processes and plume-ridge interaction from comprehensive study of the FAMOUS and North Famous segments, Mid-Atlantic Ridge. Earth and Planetary Science Letters 365, 209–220.

Gee, M.A.M., Taylor, R.N., Thirlwall, M.F., Murton, B.J., 1998a. Glacioisostacy controls the chemical and isotopic characteristics of tholeiites from Reykjanes Peninsula, SW Iceland. Earth and Planetary Science Letters 164, 1–5.

Gee, M.A.M., Thirlwall, M.F., Taylor, R.N., Lowry, D., Murton, B.J., 1998b. Crustal processes: Major controls on Reykjanes peninsula lava chemistry, sw Iceland. Journal of Petrology 39, 819–839.

Ghiorso, M.S., 1997. Thermodynamic models of igneous processes. Annual Reviews of Earth and Planetary Sciences 25, 221–241.

Ghiorso, M.S., Hirschmann, M.M., Reiners, P.W., III, V.C.K., 2002. The pMELTS: A revision of MELTS for improved calculation of phase relations and major element partitioning related to partial melting of the mantle to 3 GPa. Geochemistry, Geophysics, Geosystems 3.

Ghiorso, M.S., Sack, R.O., 1995. Chemical mass trasfer in magmatic processes IV. A revised and internally consistent thermodynamic model for the interpolation and extrapolation of liquid-solid equilibria in magmatic systems at elevated temperatures and pressures. Contributions to Mineralogy and Petrology 119, 197–212.

Gillis, K.M., Snow, J.E., Klaus, A., Abe, N., Álden B. Adrião, Akizawa, N., Ceuleneer, G., Cheadle, M.J., Faak, K., Falloon, T.J., Friedman, S.A., Godard, M., Guerin, G., Harigane, Y., Horst, A.J., Hoshide, T., Ildefonse, B., Jean, M.M., John, B.E., Koepke, J., Machi, S., Maeda, J., Marks, N.E., McCaig, A.M., Meyer, R., Morris, A., Nozaka, T., Python, M., Sahaand, A., Wintsch, R.P., 2014. Primitive layered gabbros from fast-spreading lower oceanic crust. Nature 505, 204–207.

Gurenko, A.A., Chaussidon, M., 1995. Enriched and primitive melts included in olivine from Icelandic tholeiites: origin by continuous melting of a single mantle column. Geochimica et Cosmochimica Acta 59, 2905–2917.

Hardarson, B.S., Fitton, J.G., 1997. Mechanisms of crustal accretion in Iceland. Geology 25, 1043–1046.

Hartley, M.E., Neave, D.A., Maclennan, J., Edmonds, M., Thordarson, T., 2015. Diffusive over-hydration of olivine-hosted melt inclusions. Earth and Planetary Science Letters 425, 168–178.

Hirschmann, M.M., Stolper, E.M., 1996. A possible role for garnet pyroxenite in the origin of the "garnet signature" in MORB. Contributions to Mineralogy and Petrology 124, 185–208.

Jenner, F.E., O'Neill, H.S.C., 2012. Analysis of 60 elements in 616 ocean floor basaltic glasses. Geochemistry, Geophysics, Geosystems 13.

Johnson, K.T.M., Dick, H.J.B., 1992. Open system melting and temporal and spatial variation of peridotite and basalt at the Atlantis II Fracture Zone. Journal Geophysical Research 97, 9219–9241.

Johnson, K.T.M., Dick, H.J.B., Shimizu, N., 1990. Melting in the oceanic upper mantle: an ion microprobe study of diopsides in abyssal peridotites. Journal Geophysical Research 95, 2661–2678.

Katz, R.F., Spiegelman, M., Langmuir, C.H., 2003. A new parametrization of hydrous mantle melting. Geochemistry, Geophysics, Geosystems 4.

Kelemen, P.B., Hirth, G., Shimizu, N., Spiegelman, M., Dick, H.J.B., 1997. A review of melt migration processes in the adiabatically upwelling mantle beneath oceanic spreading ridges. Philosophical Transactions: Mathematical, Physical and Engineering Sciences 355, 283–318.

Klein, E.M., Langmuir, C.H., 1987. Global correlations of ocean ridge basalt chemistry with axial depth and crustal thickness. Journal of Geophysical Research 92, 8089–8115.

Kogiso, T., Hirose, K., Takahashi, E., 1998. Melting experiments on homogeneous mixtures of peridotite and basalt: application to the genesis of ocean island basalts. Earth and Planetary Science Letters 162, 45–61.

Kokfelt, T., Hoernle, K., Hauff, F., Fiebig, J., Werner, R., Garbe-Schönberg, D., 2006. Combined trace element and Pb-Nd-Sr-O isotope evidence for recycled oceanic crust (upper and lower) in the Iceland mantle plume. Journal of Petrology 47, 1705–1749.

Koornneef, J.M., Stracke, A., Bourdon, B., Meier, M.A., Jochum, K.P., Stoll, B., Grönvold, K., 2012. Melting of a two-component source beneath Iceland. Journal of Petrology 53, 127–157.

Lambart, S., Laporte, D., Schiano, P., 2013. Markers of the pyroxenite contribution in the major-element compositions of oceanic basalts: review of the experimental constraints. Lithos 160–161, 14–36.

Langmuir, C.H., 1989. Geochemical consequences of *in situ* crystallisation. Nature 340, 199–205.

Langmuir, C.H., Bender, J.F., Bence, A.E., Hanson, G.N., Taylor, S.R., 1977. Petrogenesis of basalts from the FAMOUS area: Mid Atlantic Ridge. Earth and Planetary Science Letters 36, 133–156.

Langmuir, C.H., Klein, E.M., Plank, T., 1992. Petrological systematics of mid-ocean ridge basalts: Constraints on melt generation beneath ocean ridges. American Geophysical Union Monograph 71, 183–280.

Laubier, M., Gale, A., Langmuir, C.H., 2012. Melting and crustal processes at the FAMOUS segment (Mid-Atlantic Ridge: New insights from olivine-hosted melt inclusions from multiple samples). Journal of Petrology 53, 665–698.

Laubier, M., Schiano, P., Doucelance, R., Ottolini, L., Laporte, D., 2007. Olivine-hosted melt inclusions and melting processes beneath the FAMOUS zone (Mid-Atlantic-Ridge). Chemical Geology 240, 129–150.

Lissenberg, J., MacLeod, C.J., Howard, K.A., Godard, M., 2013. Pervasive reactive melt migration through fast-spreading lower oceanic crust (Hess Deep, equatorial Pacific Ocean). Earth and Planetary Science Letters 361, 436–447.

Maclennan, J., 2008a. Concurrent mixing and cooling of melts under Iceland. Journal of Petrology 49, 1931–1953.

Maclennan, J., 2008b. Lead isotope variability in olivine-hosted melt inclusions from Iceland. Geochimica et Cosmochimica Acta 72, 4159–4176.

Maclennan, J., McKenzie, D., Grönvold, K., 2001a. Plume-driven upwelling under central Iceland. Earth and Planetary Science

Letters 194, 67–82.

Maclennan, J., McKenzie, D., Grönvold, K., Shimizu, N., Eiler, J.M., Kitchen, N., 2003. Melt mixing and crystallisation under Theistareykir, northeast Iceland. Geochemistry, Geophysics, Geosystems 4.

Maclennan, J., McKenzie, D., Grönvold, K., Slater, L., 2001b. Crustal accretion under northern Iceland. Earth and Planetary Science Letters 191, 295–310.

McKenzie, D., 1985. ^{230}Th-^{238}U disequilibrium and the melting process beneath ridge axes. Earth and Planetary Science Letters 72, 149–157.

McKenzie, D., Bickle, M.J., 1988. The volume and composition of melt generated by extension of the lithosphere. Journal of Petrology 29, 625–679.

McKenzie, D., O'Nions, R.K., 1991. Partial melt distributions from inversion of rare earth element concentrations. Journal of Petrology 32, 1021–1091.

Michael, P., 1995. Regionally distinctive sources of depleted MORB: evidence from trace elements and H_2O. Earth and Planetary Science Letters 131, 301–320.

Neave, D.A., Passmore, E., Maclennan, J., Fitton, G., Thordarson, T., 2013. Crystal–melt relationships and the record of deep mixing and crystallisation in the AD Laki eruption, Iceland. Journal of Petrology 54, 1661–1690.

Nicholson, H., Condomines, M., Fitton, J.G., Fallick, A.E., Gronvöld, K., Rogers, G., 1991. Geochemical and isotopic evidence for crustal assimilation beneath krafla, Iceland. Journal of Petrology 32, 1005–1020.

O'Hara, M.J., 1968. Are ocean floor basalts primary magma? Nature 220, 683–686.

O'Hara, M.J., 1977. Geochemical evolution during fractional crystallisation of a periodically refilled magma chamber. Nature 266, 503–507.

O'Hara, M.J., Matthews, R.E., 1981. Geochemical evolution in an advancing, periodically replenished, periodically tapped, continuously fractionated magma chamber. Journal of the Geological Society of London 138, 237–277.

O'Neill, H.S.C., Jenner, F.E., 2012. The global pattern of trace-element distributions in ocean floor basalts. Nature 491, 698–704.

O'Nions, R.K., Pankhurst, R.J., 1974. Petrogenetic significance of isotope and trace element variations in volcanic rocks from the mid-atlantic. Journal of Petrology 15, 603–604.

Parai, R., Mukhopadhyay, S., 2012. How large is the subducted water flux? new constraints on mantle regassing rates. Earth and Planetary Science Letters 317–318, 396–406.

Peate, D.W., Baker, J.A., Jakobsson, S.P., Waight, T.E., Kent, A.J.R., Grassineau, N.V., Skovgaard, A.C., 2009. Historic magmatism on the Reykjanes Peninsula, Iceland: a snap-shot of melt generation at a ridge segment. Contributions to Mineralogy and Petrology 157, 359–382.

Pertermann, M., Hirschmann, M.M., 2003. Partial melting experiments on a MORB-like pyroxenite between 2 and 3 GPa: Constraints on the presence of pyroxenite in the basalt source regions from solidus location and melting rate. Journal of Geophysical Research 108.

R Core Team, 2016. R: A Language and Environment for Statistical Computing. R Foundation for Statistical Computing. Vienna, Austria.

Rubin, K.H., Sinton, J.M., 2007. Inferences on mid-ocean ridge thermal and magmatic structure from MORB compositions. Earth and Planetary Science Letters 260, 257–276.

Rubin, K.H., Sinton, J.M., Maclennan, J., Hellebrand, E., 2009. Magmatic filtering of mantle compositions at mid-ocean-ridge volcanoes. Nature Geoscience 2, 321–328.

Rudge, J.F., Maclennan, J., Stracke, A., 2013. The geochemical consequences of mixing melts from a heterogeneous mantle. Geochimica et Cosmochimica Acta 114, 112–143.

Saal, A.E., Hauri, E., Langmuir, C.H., Perfit, M., 2002. Vapour undersaturation in primitive mid-ocean-ridge basalt and the volatile content of Earth's upper mantle. Nature 419, 451–455.

Schiano, P., Allègre, C.J., Dupré, B., Lewin, E., Joron, J.L., 1993. Variability of trace elements in basaltic suites. Earth and Planetary Science Letters 119, 37–51.

Schuetzenmeister, E.M.A., Model, F., 2014. mcr: Method Comparison Regression. R package version 1.2.1.

Shimizu, N., 1998. The geochemistry of olivine-hosted melt inclusions in a FAMOUS basalt ALV519-4-1. Physics of the Earth and Planetary Interiors 107, 183–201.

Shorttle, O., 2015. Geochemical variability in MORB controlled by concurrent mixing and crystallisation. Earth and Planetary Science Letters 424, 1–14.

Shorttle, O., Maclennan, J., 2011. Compositional trends of Icelandic basalts: Implications for short-lengthscale lithological heterogeneity in mantle plumes. Geochemistry, Geophysics, Geosystems 12.

Shorttle, O., Maclennan, J., Lambart, S., 2014. Quantifying lithological variability in the mantle. Earth and Planetary Science Letters 395, 24–40.

Shorttle, O., Maclennan, J., Piotrowski, A.M., 2013. Geochemical provincialism in the Iceland plume. Geochimica et Cosmochimica Acta 122, 363–397.

Sinton, J., Grönvold, K., Sæmundsson, K., 2005. Postglacial eruptive history of the Western Volcanic Zone, Iceland. Geochemistry, Geophysics, Geosystems 6.

Sinton, J.M., Detrick, R.S., 1992. Mid-ocean ridge magma chambers. Journal of Geophysical Research 97, 197–216.

Slater, L., McKenzie, D., Gronvöld, K., Shimizu, N., 2001. Melt generation and movement beneath Theistareykir, NE Iceland. Journal of Petrology 42, 321–354.

Smith, M.C., Perfit, M.R., Fornari, D.J., Ridley, W.I., Edwards, M.H., Kurras, G.J., Damm, K.I.V., 2001. Magmatic processes and segmentation at a fast spreading mid-ocean ridge: detaiiled investigation of an axial discontinuity on the East Pacific Rise crest at 9°37′N. Geochemistry, Geophysics, Geosystems 2.

Smith, P.M., Asimow, P.D., 2005. Adiabat_1ph: A new public front-end to the MELTS, pMELTS, and pHMELTS models. Geochemistry, Geophysics, Geosystems 6.

Sobolev, A.V., 1996. Melt inclusions in minerals as a source of principle petrological information. Petrology 4, 228–239.

Spiegelman, M., Kelemen, P.B., 2003. Extreme chemical variability as a consequence of channelized melt transport. Geochemistry, Geophysics, Geosystems 4.

Stracke, A., Zindler, A., Salters, V.J.M., McKenzie, D., Blichert-Toft, J., Albarède, F., Grönvold, K., 2003. Theistareykir revisited. Geochemistry, Geophysics, Geosystems 4.

Thirlwall, M.F., Gee, M.A.M., Taylor, R.N., Murton, B.J., 2004. Mantle components in Iceland and adjacent ridges investigated using double-spike Pb isotope ratios. Geochimica et Cosmochimica Acta 68, 361–386.

van Westrenen, W., Blundy, J., Wood, B., 1999. Crystal-chemical controls on trace element partitioning between garnet and anhydrous silicate melt. American Mineralogist 84, 838–847.

Wood, B.J., Blundy, J.D., 1997. A predictive model for rare earth element partitioning between clinopyroxene and anhydrous silicate melt. Contributions to Mineralogy and petrology 129, 166–181.
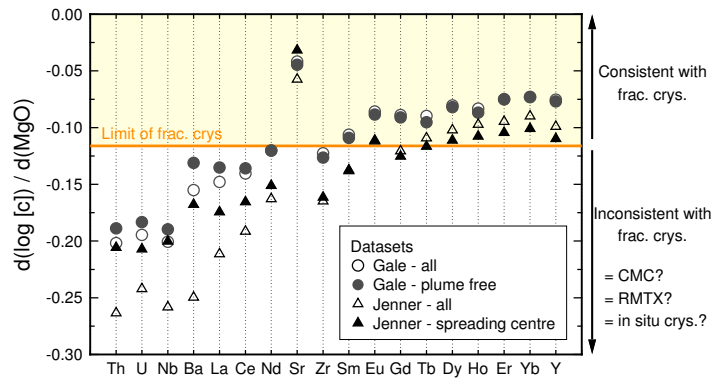
Figure 1: A characterisation of trace element over-enrichment in MORB by the slope of data in log of trace element versus MgO space. The maximum mean gradient produced by fractional crystallisation over the interval 9.5–5 wt% MgO is shown by the orange line: this was calculated assuming 70% crystallisation and $K_d = 0$. Trace elements with enrichment gradients plotting above the orange line are potentially consistent with fractional crystallisation (given appropriate K_d's etc.), whereas elements whose gradient plots below the orange line show too great an enrichment during differentiation to be produced solely by fractional crystallisation. We have calculated trace element enrichment gradients from two datasets of natural MORB, that of Gale et al. (2013a) and Jenner and O'Neill (2012). In each case we analyse both the whole dataset (in the case of the Gale et al. (2013a) just excluding back-arc basins), and a filtered dataset, excluding plume influenced sections of ridge from Gale et al. (2013a) and non-spreading centre samples from Jenner and O'Neill (2012). In the case where both datasets are filtered to represent samples from spreading centres, their calculated gradients are in reasonable agreement.
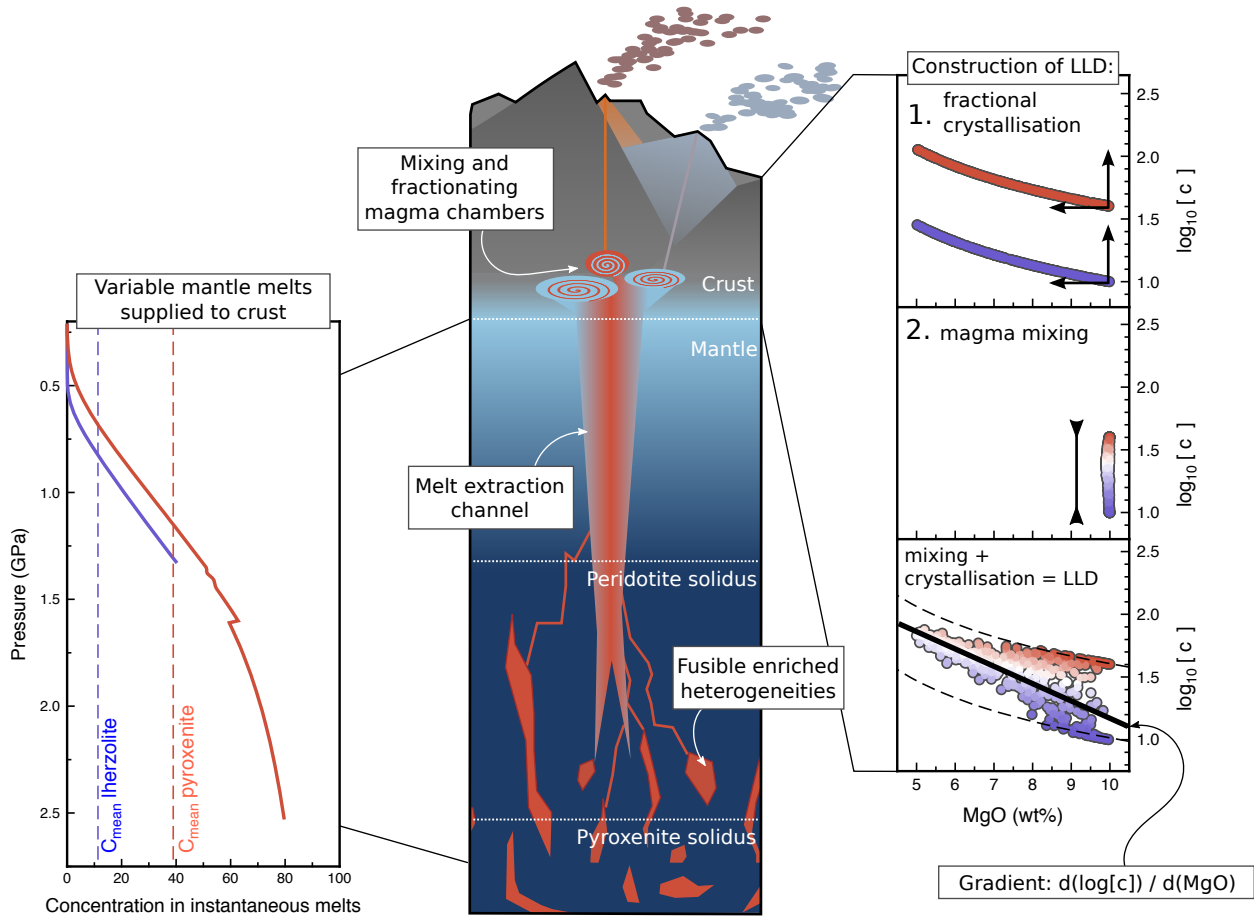
Figure 2: Schematic illustrating the processes operating from the mantle to crust that can give rise to liquid lines of descent (LLD) deviating from that predicted by simple fractional crystallisation of single magma batches. *Variable mantle melts supplied to the crust*: This panel shows the instantaneous melt compositions predicted from pMELTS calculations (Smith and Asimow, 2005; Ghiorso et al., 2002) of fractional melting using the variable partition coefficients for La from Wood and Blundy (1997); van Westrenen et al. (1999). Calculations have been performed for two lithologies, a KLB1 type lherzolite (blue) with a starting La concentration of 1 ppm and a KG1 type pyroxenite (red, Kogiso et al. (1998)) with a starting La concentration of 5.5 ppm. Vertical dashed lines indicate the mean composition of melts from both lithologies after decompression melting to the base of the crust, these compositions are used in the mixing calculations shown in the right hand panels. *Magma transport and mixing cartoon*: Melts form in the mantle from lherzolitic and pyroxenitic source lithologies producing a range of depleted–enriched primitive melts. If the chemical identity of these diverse melt batches is preserved during their travel to the surface, for example by transport in high porosity channels (Spiegelman and Kelemen, 2003), then differentiation begins with crustal magma chambers receive variably enriched and depleted magmas. *Construction of LLD*: These panels show how the processes of mixing and crystallisation combine to produce apparent LLDs that deviate from simple fractional crystallisation. In each case, log of trace element concentration is plotted against MgO for a simple case of two endmember magma compositions, enriched (red) and depleted (blue). Once resident in magma chambers, the suite of chemically variable magmas will begin to crystallise and mix. Mixing on its own destroys the primary variability of melts leaving the mantle. Fractional crystallisation, without mixing, evolves each magma along a separate path. Combining mixing and crystal fractionation produces a LLD over-enriched for depleted compositions compared with simple fractional crystallisation models.
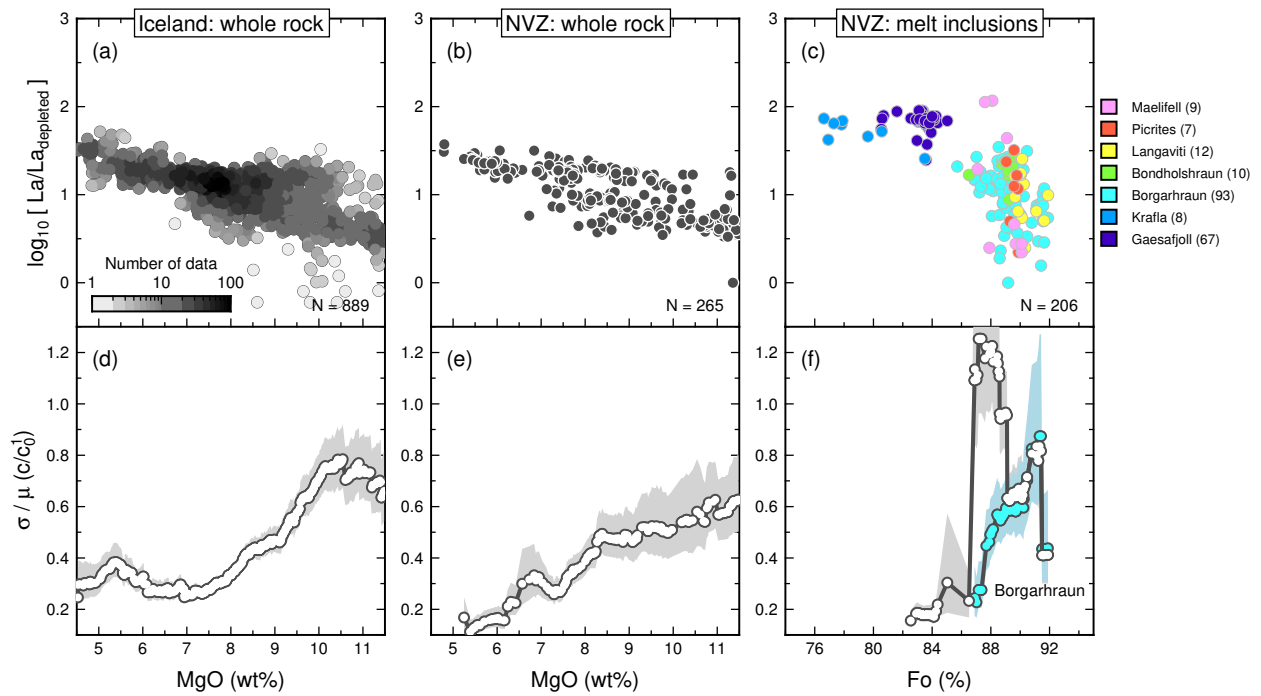
22

Figure 3: Raw whole rock, glass and melt inclusion datasets from Iceland, showing crustal mixing and fractionation processes. From left to right panels (a)–(c) narrow their spatial focus, from all Iceland's rift zones (~ 300 km), to the northern volcanic zone's Theistareykir and Krafla volcanic systems (NVZ, ~ 90 km), to individual suites of melt inclusions from the NVZ. In the upper panels (a–c) log of La concentration ratioed to the most depleted compositions in each dataset is plotted against an index of differentiation, either MgO in the case of whole rock, or forsterite content of host olivine (Fo) for the melt inclusions. La was chosen as being sensitive to both variability inherited from the melting process and mantle heterogeneity (Fig. 2), and due to its incompatible behaviour during low pressure differentiation. In (a) points are coloured according to their number density in $\log_{10}[La/La_{depleted}]$–MgO space, so that the data distribution is visible. The bottom panels (d)–(f) record the relative variability of raw La as a function of MgO, where σ is the standard deviation and μ the mean. For whole rock and glass datasets, σ/μ was calculated in a moving boxcar window of width 1 wt%, for melt inclusion datasets the window was 2 Fo units; in each case the parameters were only calculated in bins with > 5 samples. For the melt inclusion records in (c) and (f), points have been coloured according to the sample they are from (given in key). Shaded regions around each profile record the 95% confidence interval on the estimate of σ/μ. Data sources are listed in the appendix.
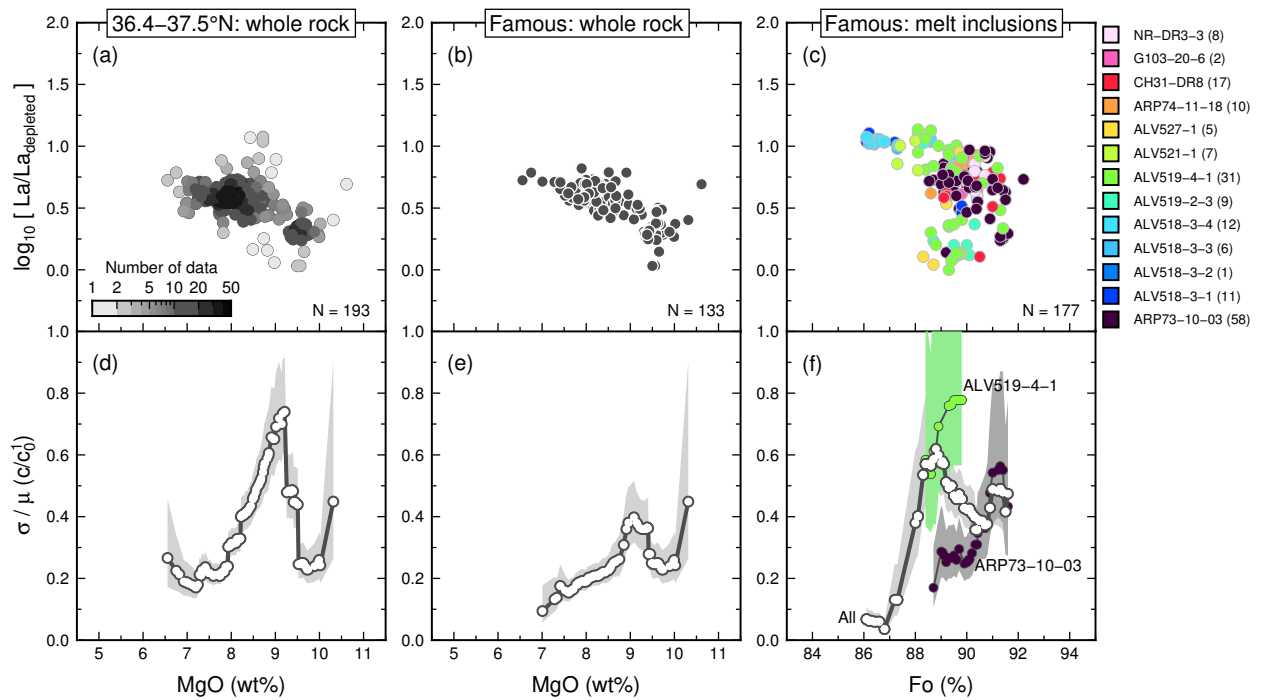
Figure 4: Equivalent plots to Fig. 3, but for the Famous region of the Mid-Atlantic Ridge. Again, the spatial scales considered narrow from (a)–(c), from a ~ 200 km length of the Mid-Atlantic Ridge around the Famous segment, to the Famous segment itself (~ 45 km, Laubier et al. (2012)), to sample specific melt inclusion suites from the Famous segment. In the lower panels the evolution of geochemical variability during differentiation is tracked. For whole rock and glass datasets σ/μ was calculated in a moving boxcar window of width 1 wt%, for melt inclusion datasets the window was 1 Fo units. For the melt inclusion records in (c) and (f), points have been coloured according to the sample they are from (given in key). Shaded regions around each profile record the 95% confidence interval on the estimate of σ/μ. Famous data from Gale et al. (2013b); Laubier et al. (2012, 2007); Shimizu (1998).
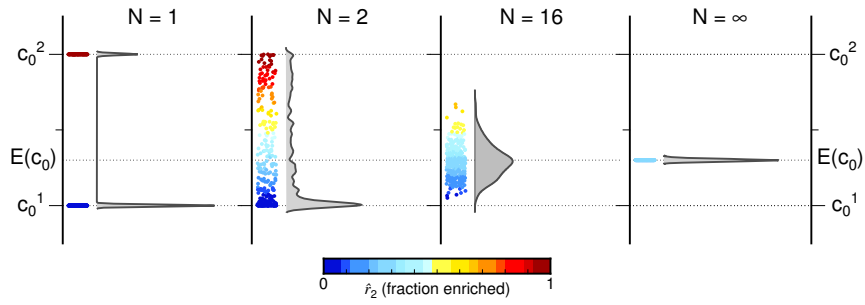
Figure 5: An illustration of how the Dirichlet mixing parameter N translates into the distribution of randomly generated samples when mixing is considered on its own (i.e. no fractional crystallisation). Two initial melts have been defined with arbitrary composition, a depleted melt $C_0^{(1)}$ and an enriched melt $C_0^{(2)}$. Three hundred samples, derived from these parental compositions by random mixing according to the Dirichlet distribution ($\mathrm{Dir}(\frac{3}{10}(N-1), \frac{7}{10}(N-1))$, equation 11), are plotted as circles (arbitrary x position) and coloured by the proportion of each parental melt in the mixture. A kernel density estimate of the sample distribution is also plotted in grey. The parental melts are present in the proportion 70:30 depleted:enriched ($\omega_2 = 0.3$). The degree of mixing increases from left to right between the plots, which causes the diminishing dispersion of the randomly drawn samples. When $N = 1$ no mixing takes place and a sample randomly drawn from the distribution will have the same composition as either of the two endmembers, with a probability weighted by the mass proportion of the endmember melts, ω (hence the area of the $C_0^{(2)}$ kernel density estimate is $\sim 3/7$ the area of the $C_0^{(1)}$ kernel density estimate). When $N > 1$ mixing between the endmember compositions will occur, and samples are distributed between the two extremes. As $N \to \infty$ mixing becomes ever more efficient, and any given sample tends towards the mean composition of the system $\widehat{C}_0 \to \mathbb{E}(\widehat{C}_0) = \overline{C}_0$.
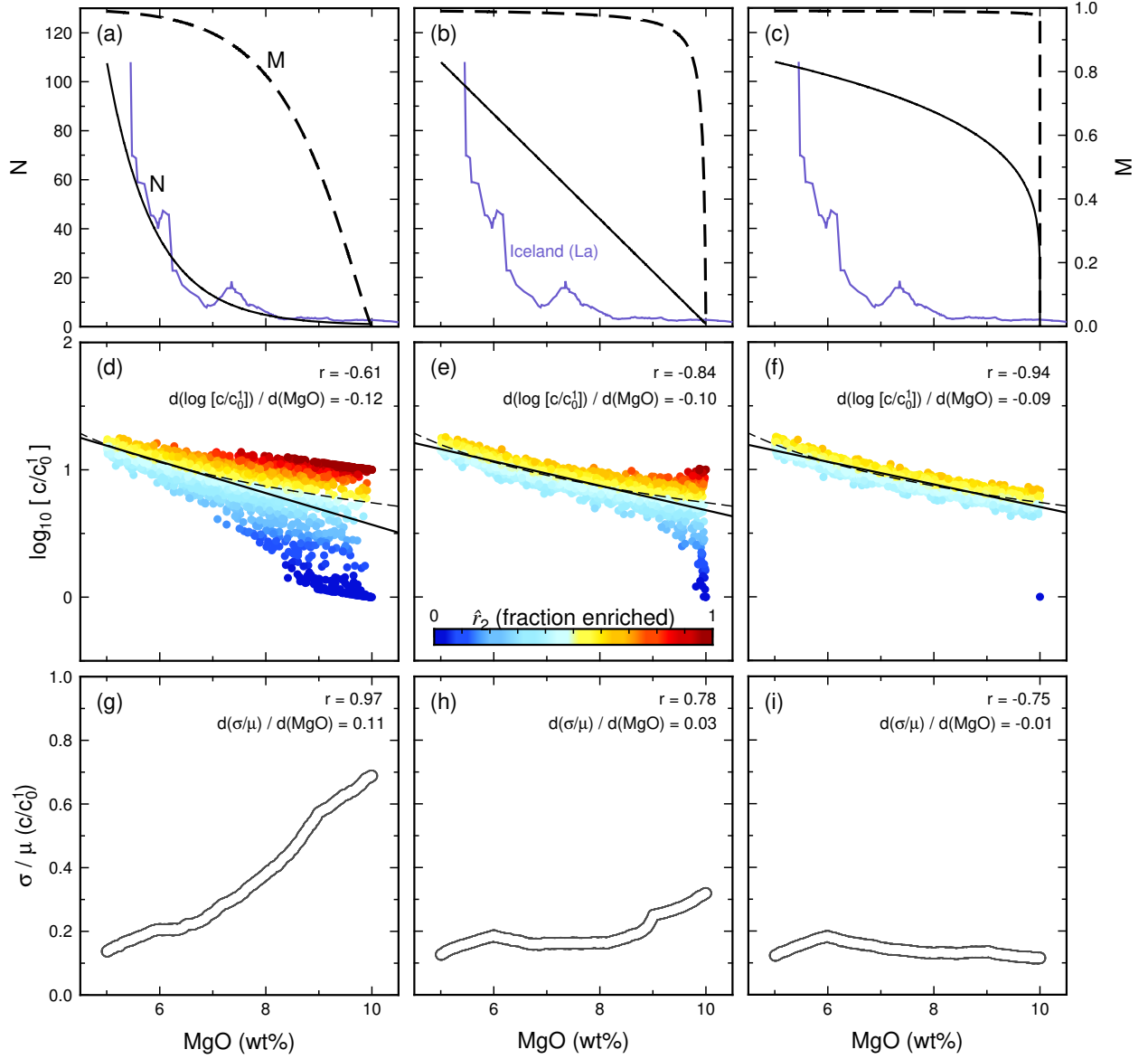
Figure 6: Testing how the rate of mixing during differentiation affects concurrent mixing and crystallisation in trace element–MgO space. (a)–(c) Investigate three different mixing scenarios, where significant mixing (M, dashed line) occurs increasingly early during differentiation. The Dirichlet mixing parameter N is also plotted as a solid line and is inversely proportional to the variability preserved in a chemical parameter, C, and related to M by $M = 1 - 1/N$ (Rudge et al., 2013). In terms of the Dirichlet mixing parameter (a) and (c) represent choices of k from equation 3 of 1.2 and 0.05 respectively, whereas (b) presents a linear model $\widehat{N} = N_{\max} - (N_{\max} - N_{\min})\widehat{U}$. The solid blue line is the value of N calculated from the variance–MgO profile of Icelandic whole rock data for Nb (Shorttle et al., 2014), scaled between $N = 1$–108. (d)–(f) Show synthetic distributions of data for these three cases of mixing. Two primary melt compositions (C_0^1 and C_0^2) present in equal proportions ($\omega_1 = \omega_2 = 0.5$), but with different starting concentrations ($C_0^2/C_0^1 = 10$), are mixed according to the corresponding N(MgO) relationship. Points are plotted normalised to the composition of the primitive depleted melt and are coloured by the contribution of enriched melt in the mixture ($\hat{r}_2$). The dashed line records simple fractional crystallisation of a perfectly incompatible trace element, starting at the mean composition of the primitive melts. The solid black line is the linear regression obtained for the synthetic data, giving $d(\log[C/C_0^1])/d(\text{MgO})$. (g)–(i) Track how variability in the raw concentration of C varies during differentiation. Variability is calculated as the standard deviation (μ) in a moving boxcar filter of width 1 wt% MgO and normalised to the mean of that window (μ). A simple linear regression through these profiles gives $d(\sigma/\mu)/d(\text{MgO})$.
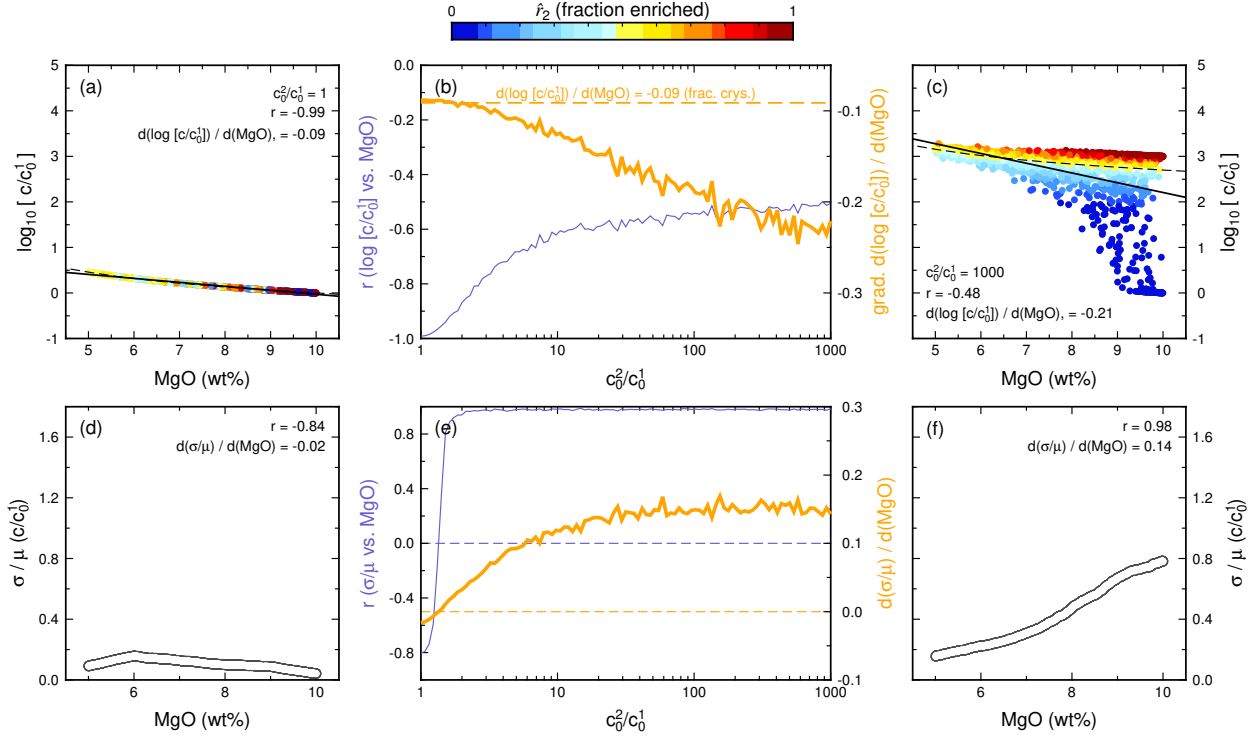
26

Figure 7: The sensitivity of the apparent trace element liquid line of descent to the initial variability in trace element concentrations entering the crust, C_0^1/C_0^2. (a) Shows the synthetic data distribution in endmember case where the enriched and depleted melts have the same concentration of a fictive element trace element 'C' (i.e. $C_0^1 = C_0^2$). In this case the data record differentiation according to simple fractional crystallisation (dashed black line, $K_d = 0$), and a linear regression through the data (solid black line) is roughly parallel to this fractionation trend. (b) The gradient $d(\log[C/C_0^1])/d(\text{MgO})$ is calculated for a range of C_0^2/C_0^1, from $C_0^2/C_0^1 = 1$–1000, and plotted as the thick orange line. The dashed orange line indicates the mean gradient of a simple fractional crystallisation trend, calculated from equation 2. The correlation coefficient between log of concentration and MgO is drawn as a thin blue line. (c) Plots the results of the synthetic mixing model at the opposite extreme, where now $C_0^2/C_0^1 = 1000$. (d)–(f) Replicate the above panels, but now for the variability–MgO profiles. Where $d(\sigma/\mu)/d(\text{MgO})$, the mixing gradient, is the gradient of the running boxcar profile of σ/μ as a function of MgO. When $d(\sigma/\mu)/d(\text{MgO}) > 0$ variability in the raw trace element concentration decreases during differentiation as predicted by CMC.
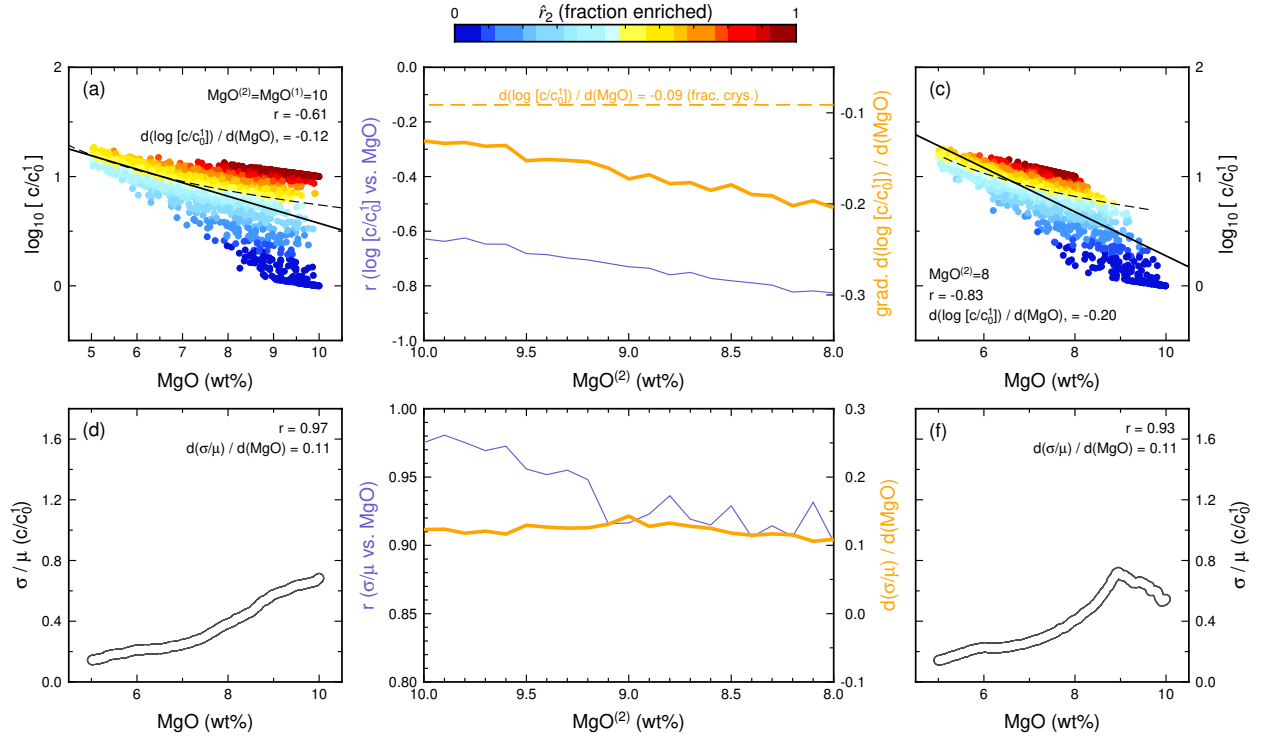
Figure 8: The sensitivity of the apparent trace element liquid line of descent to the MgO of the enriched endmember going into the mixture. (a) Shows the synthetic data distribution in endmember case where the depleted and enriched melts have the same MgO ($MgO_0^{(1)} = MgO_0^{(2)} = 10$). In all cases $\omega_1 = \omega_2 = 0.5$ and $C_0^2/C_0^1 = 10$, meaning that all solutions produce trace element–MgO distributions deviating from the case of simple fractional crystallisation (dashed line, $K_d = 0$). A linear regression through the data is shown as a solid black line. In (b) the gradient from simple linear regression, $d(\log[C/C_0^1])/d(MgO)$, is calculated for a range of enriched melt MgO ($MgO_0^{(2)}$), from $MgO_0^{(2)} = 10$–8 wt%, and plotted as the thick orange line. The dashed orange line indicates the mean gradient of a simple fractional crystallisation trend. The correlation coefficient between log of trace element concentration and MgO is drawn as a thin blue line. (c) Plots the results of the synthetic mixing model at the opposite extreme, where now $MgO_0^{(2)} = 8.0$ wt%. (d)–(f) Replicate the above panels, but now for the variability–MgO profiles. Where $d(\sigma/\mu)/d(MgO)$ is the gradient of the running boxcar profile of σ/μ as a function of MgO. When $d(\sigma/\mu)/d(MgO) > 0$, variability in the raw trace element concentration decreases during differentiation, which is true for all for all values of $MgO_0^{(2)}$.
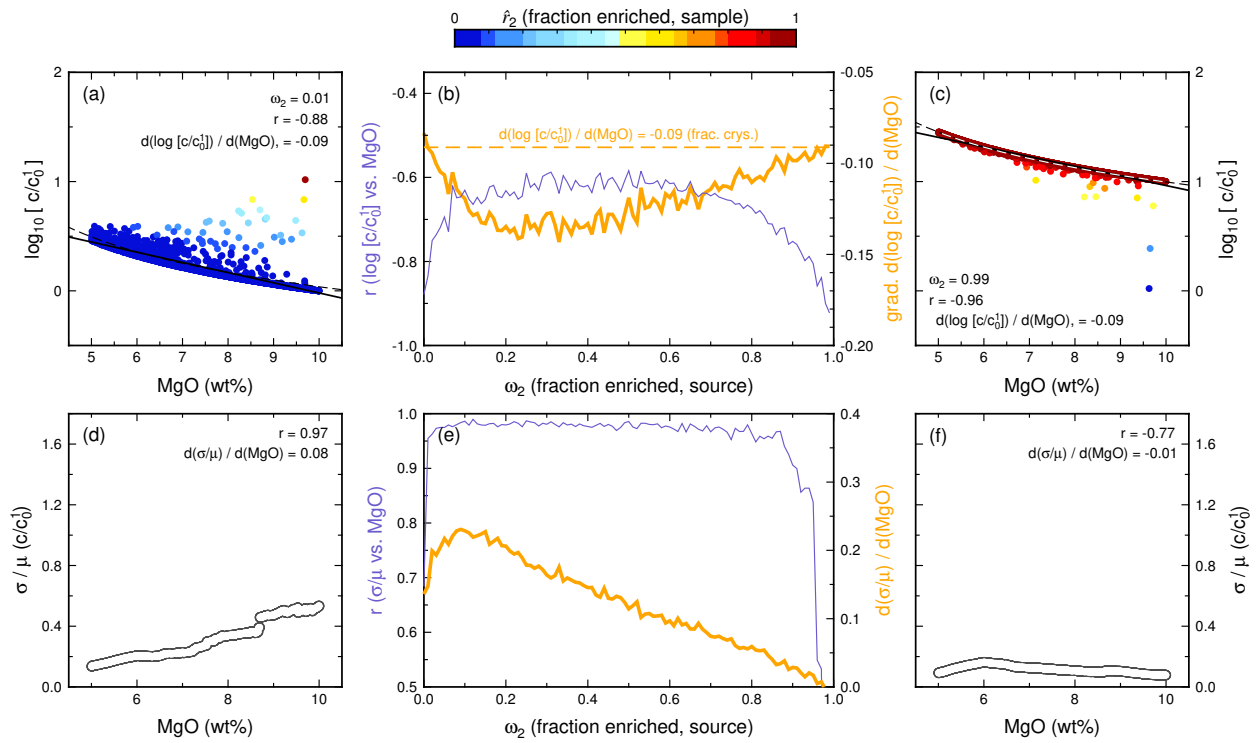
Figure 9: The sensitivity of the apparent trace element liquid line of descent to the mass fraction of enriched (ω_2) and depleted endmembers melts in the system. (a) Shows the synthetic data distribution in endmember case where the depleted melts are overwhelmingly dominant compared with the enriched melts ($\omega_2 = 0.01$). In this case the data record a differentiation trend close to simple fractional crystallisation (dashed line, $K_d = 0$), and a linear regression through the data (solid black line) is close to parallel with this fractionation trend. (b) The gradient $d(\log[C/C_0^1])/d(\text{MgO})$ is calculated for a range of ω_2, from 0.01–0.99, and plotted as the thick orange line. The dashed orange line indicates the mean gradient of a simple fractional crystallisation trend. The correlation coefficient between log of trace element concentration and MgO is drawn as a thin blue line. (c) Plots the results of the synthetic mixing model at the opposite extreme, where now $\omega_2 = 0.99$. (d)–(f) Replicate the above panels, but now for the variability–MgO profiles. Where $d(\sigma/\mu)/d(\text{MgO})$ is the gradient of the running boxcar profile of σ/μ as a function of MgO. When $d(\sigma/\mu)/d(\text{MgO}) > 0$, variability in the raw trace element concentration decreases during differentiation, which is true for all ω.
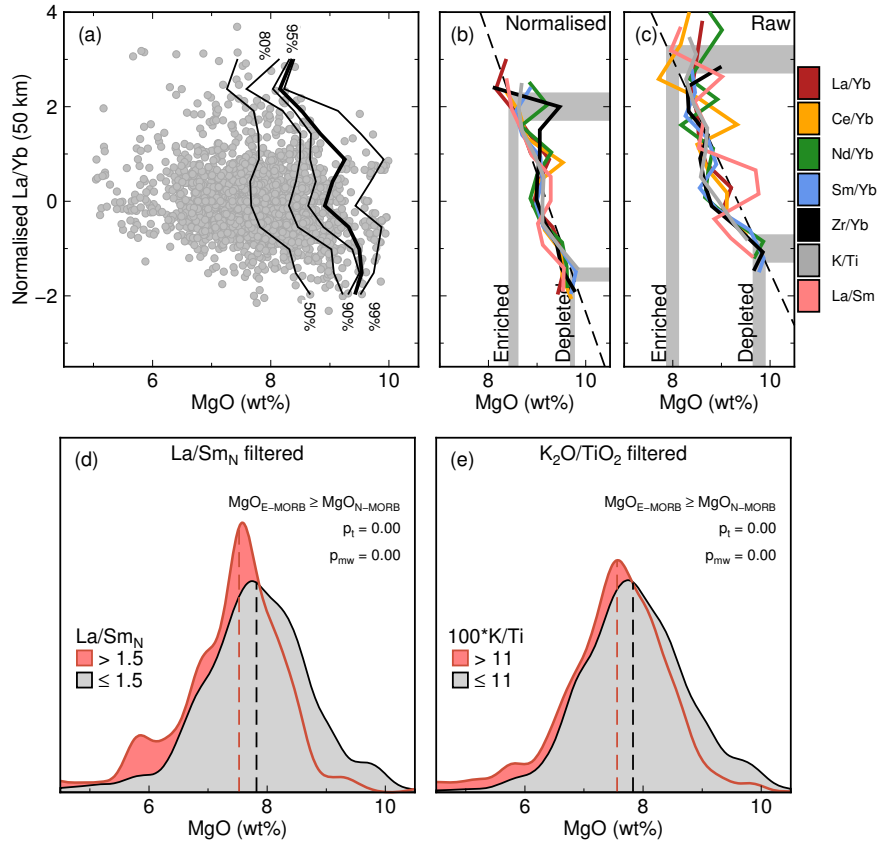
29

Figure 10: Assessing the MgO content of primitive enriched (e.g. high La/Yb) and depleted (e.g. low La/Yb) MORB. In (a) 2057 MORB from Gale et al. (2013a) are plotted as geographically normalised La/Yb vs. MgO. The geographic normalisation at a lengthscale of 50 km is calculated by subtracting a local mean and dividing by a local standard deviation. This produces a scaled dimensionless variable recording deviation of samples from the local mean composition of basalts, accounting for differences in the average degree of enrichment or depletion between localities (see Shorttle (2015) for details). To find whether there is a slope to the high MgO side of the data, i.e., whether enriched samples lie at a systematically different MgO to depleted samples, we have calculated percentiles of MgO as a function of La/Yb. These MgO percentiles are plotted as black lines split into bins of normalised La/Yb 0.5 wide: i.e. the 95% contour at a given La/Yb marks the MgO at which 95% of samples fall to lower MgO. In order to present multiple elements at once we have plotted just these 95% MgO contours for a range of normalised trace and minor element ratios in (b). Their inclination towards low MgO at high incompatible trace element ratio indicates that the most primitive enriched basalts have lower MgO than depleted basalts. The dashed black line shows the average of each of the 95% contours, and has been used at the high and low ends to define the MgO of enriched and depleted melts (vertical grey bars). The raw data (all points scaled equally without geographic normalisation) can also be used the estimate the MgO of primitive enriched and depleted melts (c). Comparing the whole dataset split into enriched and depleted groupings also shows evidence of an offset in the MgO between enriched and depleted melts. Both splitting MORB data based on their primitive mantle normalised La/Sm (d) and on K/Ti (e) (Gale et al., 2013a; Smith et al., 2001), the distribution of enriched basalts (in red) is offset to lower MgO. Calculating the one-sided students t-test (p_t) or Mann-Whitney test (p_{mw}), returns p-values rejecting the null-hypothesis that enriched MORB have either the same or greater MgO as the normal MORB at a >95% confidence level.
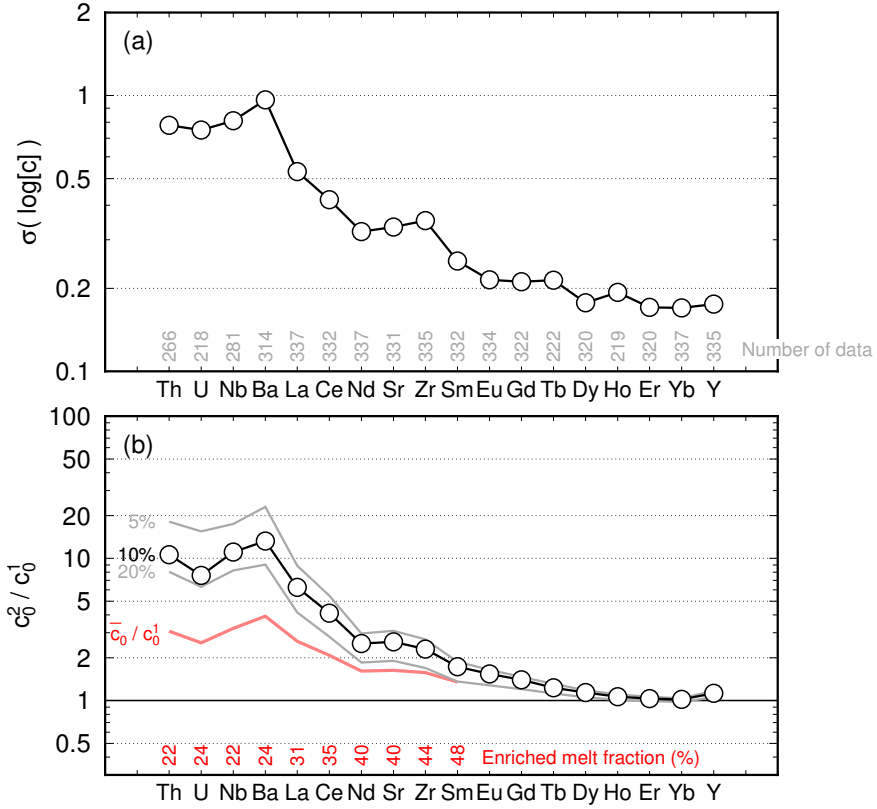
Figure 11: Assessing the variability of primitive MORB. (a) MORB from Gale et al. (2013a) with > 8.5 wt% MgO have been selected and used to calculate the log-normal variability for a range of trace elements. Where $\sigma(\log[C])$ is the standard deviation of the natural log of the trace element concentration. Grey numbers record the number of samples included in the calculation, which varies by data availability. (b) For the same set of MORB, the concentration ratio, C_0^2/C_0^1, between enriched and depleted primitive melts has been calculated. First, the La/Yb for each sample is used to group samples into upper (enriched) and lower (depleted) percentiles. C_0^2/C_0^1 is then estimated for each element by dividing its concentration in an upper percentile group (the enriched melts) by its concentration in the lower percentile group (depleted melts). Ratios are calculated for the $80^{th}/20^{th}$, $90^{th}/10^{th}$ and $95^{th}/5^{th}$ percentiles. Of these, the $90^{th}/10^{th}$ ratio is used to define C_0^2/C_0^1 in subsequent calculations. The red line gives the normalised mean composition of primitive MORB, $\bar{C}_0/C_0^1$. Mass balance between C_0^2, C_0^1, and $\bar{C}_0$ for the most incompatible elements gives an estimate of ω_2, the enriched melt fraction. These estimates of ω_2 are written in red along the horizontal axis.
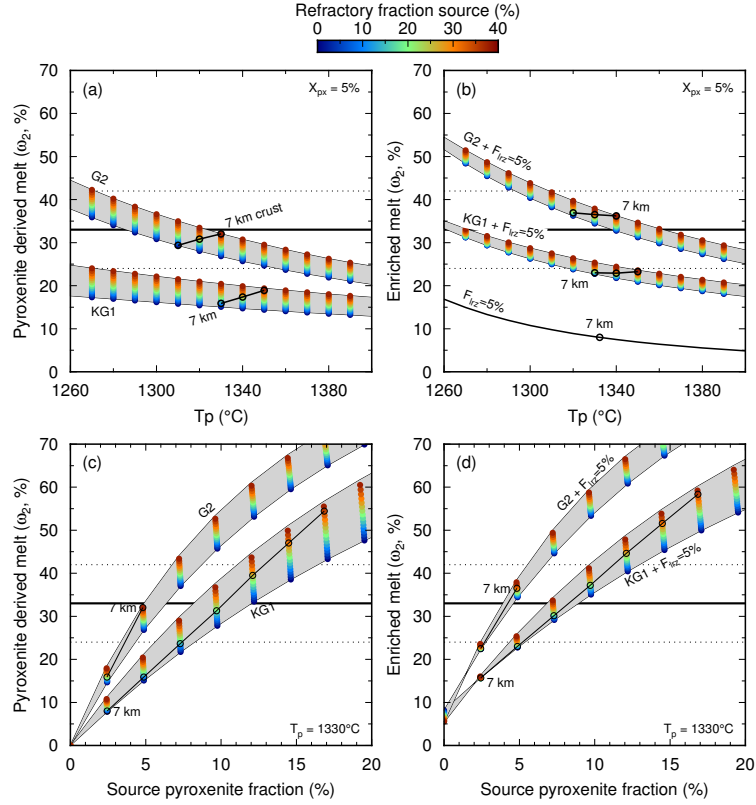
31

Figure 12: Estimating the relative proportion of enriched and depleted melts forming typical mid-ocean ridge crust, i.e. the ω_2 parameter for the mixing models. (a) Tri-lithology melting calculations have been performed using the model of Shorttle et al. (2014) over a range of mantle potential temperatures. At each temperature results are plotted for a mantle containing 5% by mass of recycled pyroxenite Hirschmann and Stolper (1996) and variable proportions of lherzolite and harzburgite (symbols coloured by harzburgite mass fraction). Calculations have been performed for the melting of two pyroxenite lithologies, the Kogiso et al. (1998) KG1 pyroxenite lithology and the Pertermann and Hirschmann (2003) G2 MORB like eclogite. Lherzolite melting is parameterised from Katz et al. (2003). The solutions for each lithology that produce the typical oceanic crustal thickness of 7 km are labelled. The thick horizontal black line in this and other panels is the estimate of ω_2 from mass balancing enriched and depleted parental melts with the mean primitive melt composition (described in the main text). Dotted lines either side are the range on this estimate. (b) Shows the results of the same calculations, but adding the first 5% of melts from the lherzolite to the melts of the pyroxenites, making the hybrid enriched melt required to match observations of binary mixing systematics in Rudge et al. (2013). The thin black line records the mass fraction of total melt production comprised by just the first 5% of melts from a single lithology lherzolite mantle. This scenario gives a lower bound on enriched melt mass fraction for the case of a lithologically homogeneous lherzolite mantle. In (c) and (d) the mass fraction of pyroxenite in the source has been varied at a constant mantle potential temperature of 1330°C, again considering a range of harzburgite fractions in the source.

Table 1: Mineral melt partition coefficients used in crystallisation calculations, after O'Neill and Jenner (2012).

Element	$D_{Olivine}$	$D_{Clinopyroxene}$	$D_{Plagioclase}$
Th	0	0.014	0.001
U	0	0.0127	0.001
Nb	0.0003	0.004	0.1
Ba	0	0.0058	0.27
La	0.00001	0.081	0.0348
Ce	0.00002	0.129	0.0278
Nd	0.0001	0.267	0.0179
Sr	0000	0.06	1.6
Zr	0.0005	0.12	0.009
Sm	0.0004	0.417	0.0132
Eu	0.0007	0.479	0.0221
Gd	0.001	0.531	0.0125
Tb	0.003	0.550	0.0120
Dy	0.004	0.596	0.0112
Ho	0.008	0.5965	0.0114
Er	0.01	0.597	0.0116
Yb	0.021	0.558	0.0155
Y	0.00776	0.7	0.001
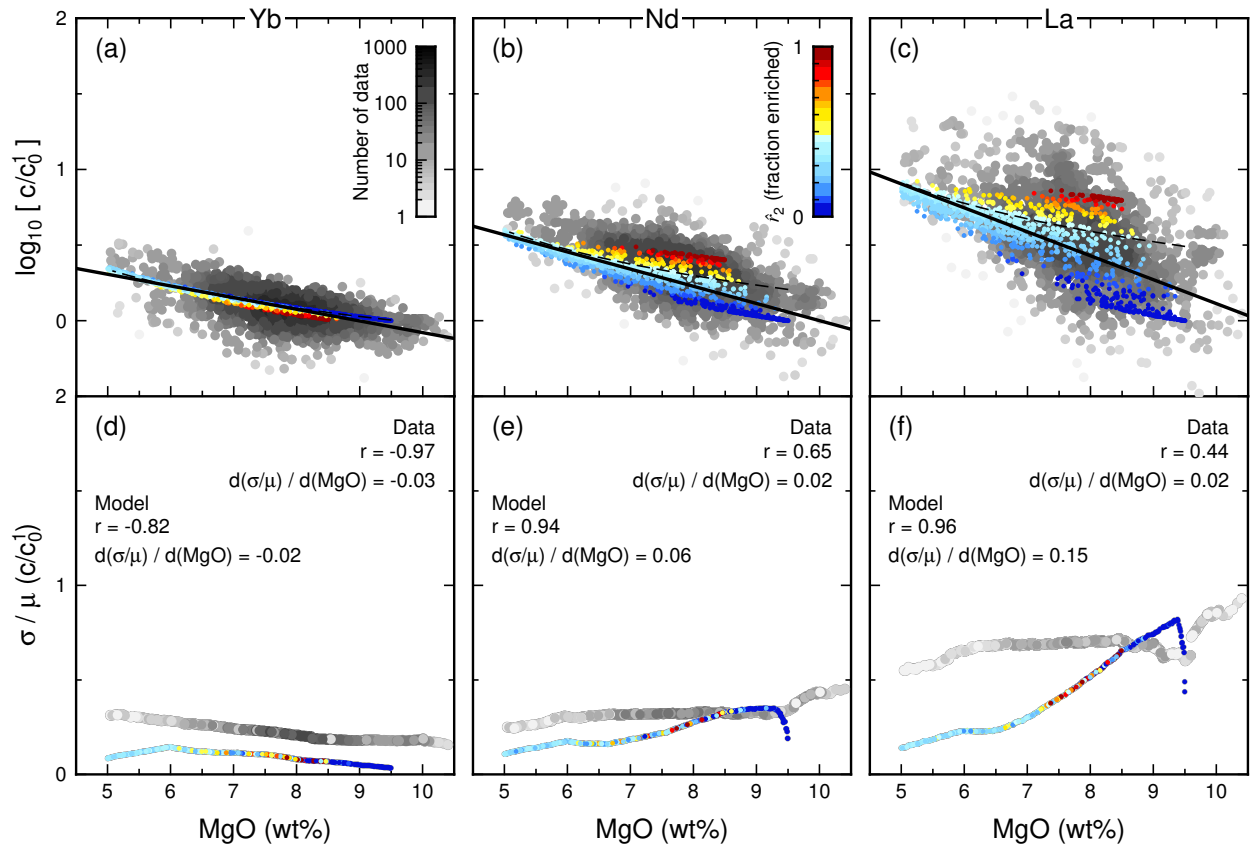
Figure 13: The results of running the mixing calculations using the parameters C_0^2/C_0^1, ω_2 and $MgO_0^{(2)}$ estimated from the real MORB data. (a)–(c) Show the raw MORB data in grey, shaded by the number density of points on the plot (data from Gale et al. (2013a)). These are overlain by the data distribution calculated from the mixing model, coloured by the mass proportion of enriched endmember in the mixture. The thin dashed line records a simple fractional crystallisation trend for each element, assuming bulk partition coefficients given in Table 1 and the relative proportion of crystallising phases 18:42:41, olivine:clinopyroxene:plagioclase, as used by O'Neill and Jenner (2012). In the lower panels (d)–(f), the running boxcar profile of σ/μ as a function of MgO has been calculated for the real and synthetic datasets.
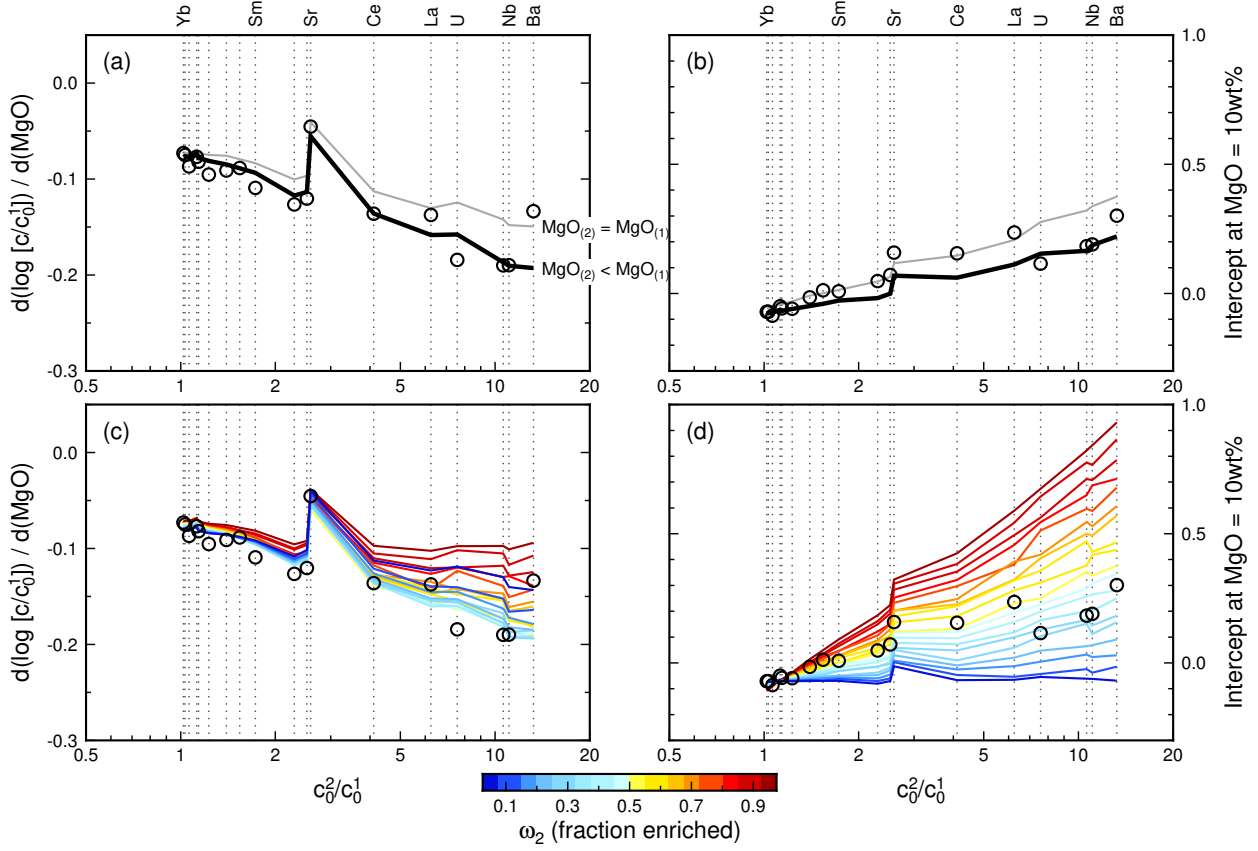
Figure 14: A comparison of the gradients and intercepts of regressions through the real MORB data in log trace element–MgO space, to the predictions from our mixing model. (a) Compares the gradient $d(\log[C/C_0^1])/d(\text{MgO})$ of the natural MORB data from Gale et al. (2013a) (circles, using the whole dataset) and model results (thick black line, $\omega_2 = 0.4$, $\text{MgO}_0^{(2)} = 8.5$ wt% and $\text{MgO}_0^{(2)} = 9.5$ wt%) as a function of the enriched to depleted concentration ratio, C_0^2/C_0^1, for each element. The thin grey line shows the result for the scenario where $\text{MgO}_0^{(2)} = \text{MgO}_0^{(1)} = 9.5$. (b) A comparison between the observed and modelled intercepts of regressions in log trace element–MgO space. (c) And (d) show the same MORB parameters as in the panels above, but with the model results reproduced for a range of enriched melt mass fractions, ω_2, from 0.05 to 0.95. For these calculations $\text{MgO}_0^{(2)} = 8.5$ wt% and $\text{MgO}_0^{(2)} = 9.5$ wt%.
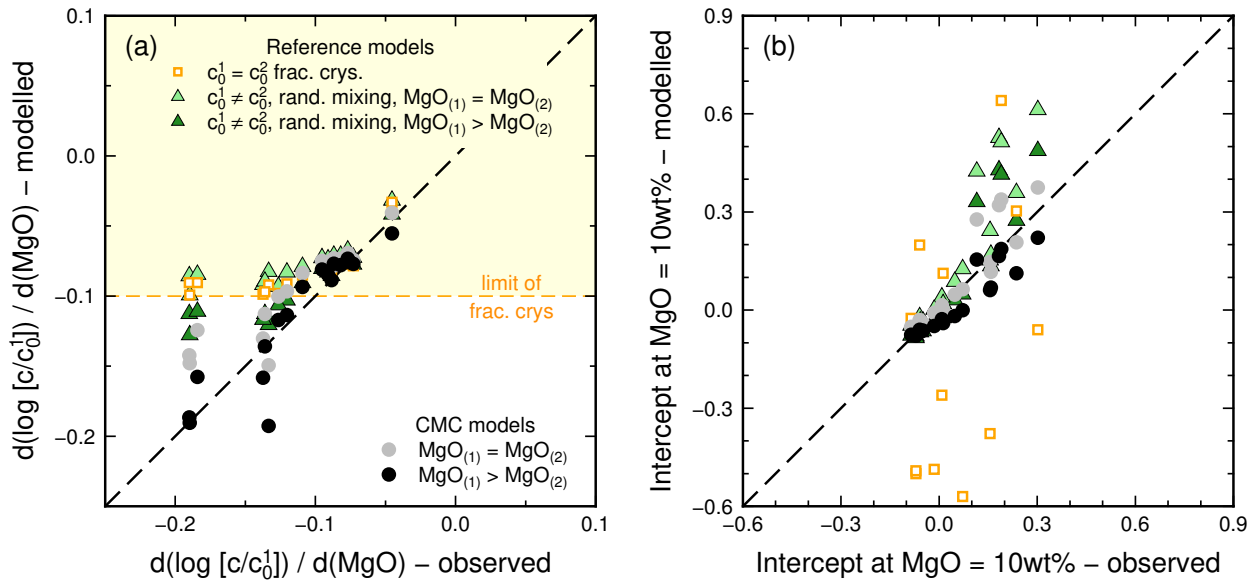
35

Figure 15: The model results compared to the observed regression parameters for the same range of trace elements plotted in Fig. 1 from the Gale et al. (2013a) dataset. Black symbols are results from the CMC model runs, where the MgO of the depleted melts $(\mathrm{MgO}_0^{(1)} = 9.5 \text{ wt\%})$ was greater than that of the enriched melt $(\mathrm{MgO}_0^{(1)} = 8.5 \text{ wt\%})$. Grey symbols are from CMC models where $\mathrm{MgO}_0^{(1)} = \mathrm{MgO}_0^{(2)} = 9.5$ wt%. Orange squares are the gradients and intercepts obtained for regression through model runs with just fractional crystallisation of a single melt composition $(\mathrm{C}_0^1 = \mathrm{C}_0^2)$. Triangles represent model runs where mixing was set to occur randomly and independently of the degree of differentiation. For these runs, light green triangles represent the case where $\mathrm{MgO}_0^{(1)} = \mathrm{MgO}_0^{(2)} = 9.5$ wt% and dark green triangles where $\mathrm{MgO}_0^{(1)} = 9.5$ wt% and $\mathrm{MgO}_0^{(2)} = 8.5$.

Table 2: Summed misfit (SS) between the various model predictions of gradient ($d(\log[C])/d(\mathrm{MgO})$) and intercept, and those parameters observed in 18 trace element–MgO pairs from the Gale et al. (2013a) suite of global MORB. Misfits have been scaled by our preferred model case: CMC, where $\mathrm{MgO}_0^{(2)} \neq \mathrm{MgO}_0^{(1)}$. The 'Mix–Crys' models are those where mixing occurred independently of crystallisation.

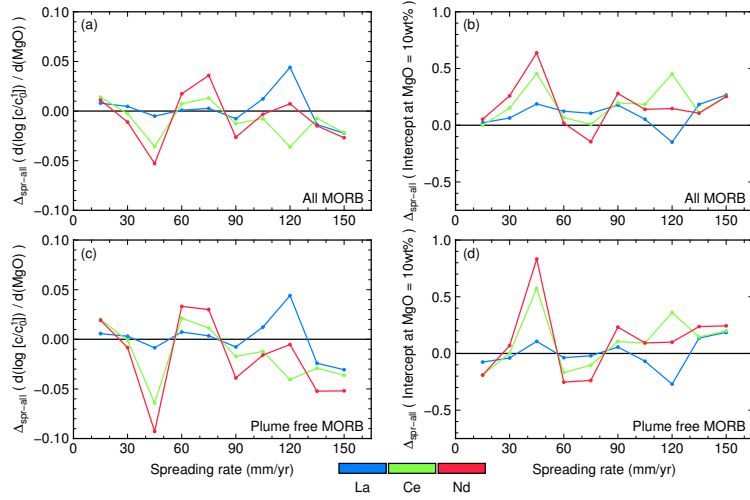| Model type	$C_0^{(i)}$	$\mathrm{MgO}_0^{(1)}$ (wt%)	$\mathrm{MgO}_0^{(2)}$ (wt%)	$SS_{d(\log[C])/d(\mathrm{MgO})}$	$SS_{intercept}$
Frac. crys.	$C_0^1 = C_0^2$	9.5	9.5	6.3	296
Mix–Crys.	$C_0^1 \neq C_0^2$	9.5	9.5	7.4	8.0
Mix–Crys.	$C_0^1 \neq C_0^2$	9.5	8.5	3.2	3.5
CMC	$C_0^1 \neq C_0^2$	9.5	9.5	2.1	1.4
CMC	$C_0^1 \neq C_0^2$	9.5	8.5	1.0	1.0

Figure 16: An assessment of whether trace element enrichment trends during differentiation differ systematically according to melt supply, for which spreading rate is taken as a proxy. In (a) and (b) the Gale et al. (2013a) global MORB dataset has been sub-sampled according to spreading rate (30 mm/yr wide bins) and the regression parameters in log trace element MgO space calculated for three incompatible trace elements (La, Ce and Nd). These elements were chosen as they show strong over-enrichment trends and they are abundantly analysed in the MORB dataset. In all panels the gradient $(d(\log[C/C_0^1])/d(\mathrm{MgO}))$ and intercept (at 10 wt% MgO) are plotted with respect to the value obtained regressing the whole dataset without sub-division according to spreading rate (and as are such prefixed with Δ_{all}). In (c) and (d) the results are presented when plume influenced sections of ridge are filtered out (Gale et al., 2013a): the elevated mantle potential temperatures associated with plumes could modify the simple melt flux–spreading relationship assumed for this analysis.

38

Trace element enrichment gradients: Definition and calculation

The analysis in this paper considers trace element over enrichment during differentiation in $\log(C/C_0^1)$ vs. MgO space, where C is the concentration of the element of interest, and C_0^1 a constant normalising factor equal to the element's concentration in a depleted endmember melt. One reason for choosing to plot the log of the trace element is for consistency with the analysis of O'Neill and Jenner (2012). O'Neill and Jenner (2012) showed that trace elements in global MORB are distributed approximately log-normally around straight lines in log(trace element)–MgO space. Although non-linearity in log(trace element)–MgO spaces potentially arises from:

1. Using MgO as an index of differentiation, rather than directly using remaining liquid mass,
2. Plotting MgO linearly, rather than as log(MgO),

O'Neill and Jenner (2012) showed that the liquid mass over the interval 5.5–9.5 wt% MgO can be approximated as an exponential function of MgO. Choosing this functional form means that fractionation trends in $\log(C/C_0^1)$–MgO space do become linear. Here we have further simplified the relationship between the remaining mass of liquid and MgO, describing it as linear (see later in appendix). The consequence of this is that fractionation trends in $\log(C/C_0^1)$–MgO space are curved, albeit not strongly so over the differentiation interval we consider (Fig. A1).

Two gradients are considered in this study, those from linear regression through data in $\log(C/C_0^1)$–MgO space, and that of the pure fractional crystallisation trajectories. Linear regressions are calculated using the MCR package (Schuetzenmeister and Model, 2014) of the R Statistical programming language (R Core Team, 2016). Gradients from the fractional crystallisation curves are calculated as the mean over the differentiation interval (equation 2).

Data for three trace elements in Global MORB are plotted both as $\log(C/C_0^1)$ and C/C_0^1 vs. MgO in Fig. A1. These plots illustrate that a main effect of choosing to analyse the data as $\log(C/C_0^1)$ is that the spread of data to low concentrations, depleted compositions, becomes apparent; conversely, samples with high concentrations are compressed towards the bulk of the distribution (compare Fig. A1 (a) and (b)). However, the gradients obtained by linear regression and from fractional crystallisation have the same sense of difference whether $\log(C/C_0^1)$ is used or not: La and Nd consistently show that the data are steeper (over-enriched) compared with what would be predicted from fractional crystallisation (red dashed lines); whereas, for Yb the data evolve to similar or lower degrees of enrichment on differentiation than would be predicted from fractional crystallisation.

These results confirm that the basic observation of trace element over-enrichment in global MORB is not predicated upon using $\log(C/C_0^1)$.

Additional model parameters

Sampling frequency and bias: implications for resolving CMC and obtaining precise gradients

Sampling frequency

The ability to accurately resolve fractionation gradients and intercepts in datasets depends on having multiple samples distributed across a range of MgO. For individual suites of MORB this can be a challenge when MgO ranges are limited and only a small number of samples have been collected. In general, having a small number of samples will not introduce systematic bias in estimates of gradient and intercept, but it will generate significant noise in the estimates of these parameters. This is shown in Fig. A2, where in the central panels the number of samples included in the formation of a synthetic sample suite (n) is varied between 10 and 1000, and at each value of n, 2000 synthetic sample suites are generated and their gradient and intercepts calculated. Fig. A2 (b) shows that the 95% confidence bound on the gradient and intercept increases significantly when n < 100 and is greater than the natural range in $d(\log[C/C_0^1])/d(\text{MgO})$ (Fig. 1) by n $\sim$ 50.

More derived properties of a sample set, its higher moments, such as the evolution of geochemical variability (σ/μ) with MgO are even harder to resolve resolve at low n (Fig. A2 (d)–(f)). In the case of

identifying that geochemical variability decreases with increasing differentiation, the key prediction of CMC, these calculations show that sample sets with n < 100 will frequently fail to exhibit this behaviour despite its presence in the underlying population. Shorttle (2015) attempted to mitigate this problem by geographically normalising MORB, to produce a single dataset from which metrics like σ/μ can be calculated. However, the only real solution is to collect more samples, and this is likely one reason why Icelandic sample sets with abundant geochemical data display clearer CMC trends than suites from even relatively well sampled portions of submarine ridge (e.g. Fig. 4).

To minimise the variability introduced into our gradient and intercept estimates from using randomly generated datasets, all trials in this study have been performed with n = 2000. From Fig.A2B, taking n = 2000 should mean our estimates of $d(\log[C/C_0^1])/d(\mathrm{MgO})$ are stable to better than 10% of the gradient's variability across trace elements in the natural dataset.

Sampling bias

A subtler corollary of the CMC model is what differentiation trends would like if the eruptive record, or what has been sampled of the eruptive record, is biased to basalts of a particular composition. Irrespective of the composition of parental melts entering the crust, if there is no primary heterogeneity, CMC predicts that the differentiation trend cannot deviate from simple fractional crystallisation (e.g. as seen in Fig. 7 (a)). However, if

1. the magma entering the crust is chemically variable,
2. and the variable magma compositions are involved in mixing and differentiation,
3. and the available samples are biased towards enriched or depleted compositions (whether through preferential eruption, sampling, or any other reason),

then the apparent differentiation trends will deviate from fractional crystallisation. In the case where samples at a given MgO are preferentially of enriched basalts, then gradients in trace element–MgO space will appear shallower than fractional crystallisation, and shallower than a regression through the whole population of magmas were sampling/eruption unbiased (e.g. dark red points in Fig. 6 (d)). If instead samples are preferentially from depleted magmas, the differentiation trend will appear steeper than fractional crystallisation, and steeper than a regression through the whole population of magmas (e.g. dark blue points in Fig. 6 (d)).
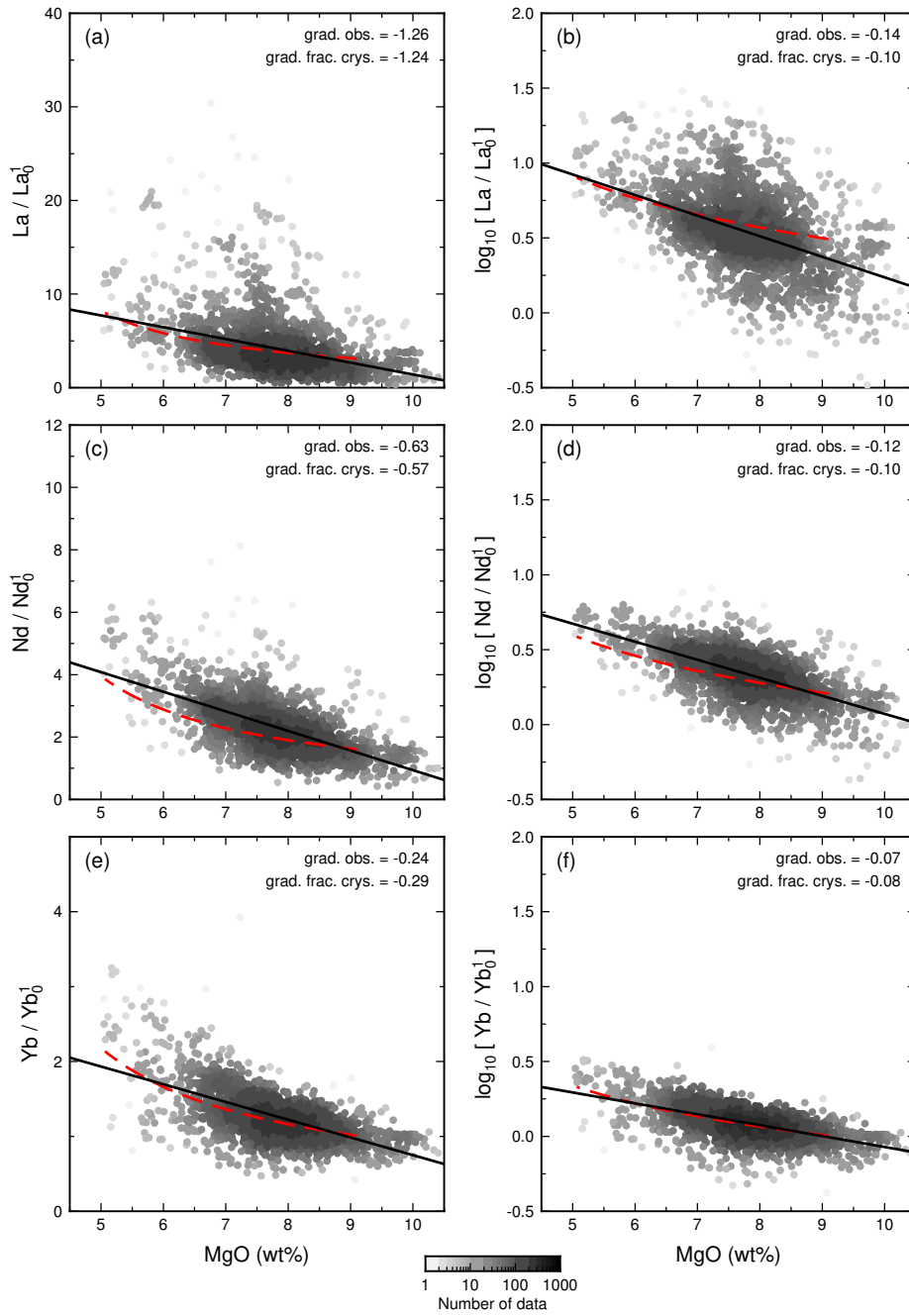
Figure A1: A comparison between trace element differentiation trends in MORB as viewed with and without taking the log of the trace element. Panels (a), (c), and (e) show the data without taking the log, just normalising all concentrations to the constant composition of the depleted endmember melt; panels (b), (d) and (f) plot log of the normalised concentrations. Differentiation trends for three trace elements of varying compatibility are shown: data for the most incompatible, La, are plotted in (a) and (b); data for Nd, which is more compatible than La, are plotted in (c) and (d); and the most compatible element of the three, Yb, is plotted in the bottom panels (e) and (f). Overlain in each panel are the results of calculating linear regression through the data (solid black line), and modelling fractional crystallisation (dashed red line). The gradients from the linear regression are given in the upper right as 'grad. obs.', and the mean gradient from fractional crystallisation are given below this as 'grad. frac. crys'. The raw MORB data are plotted in grey, shaded by the number density of points on the plot. Data are from Gale et al. (2013a).
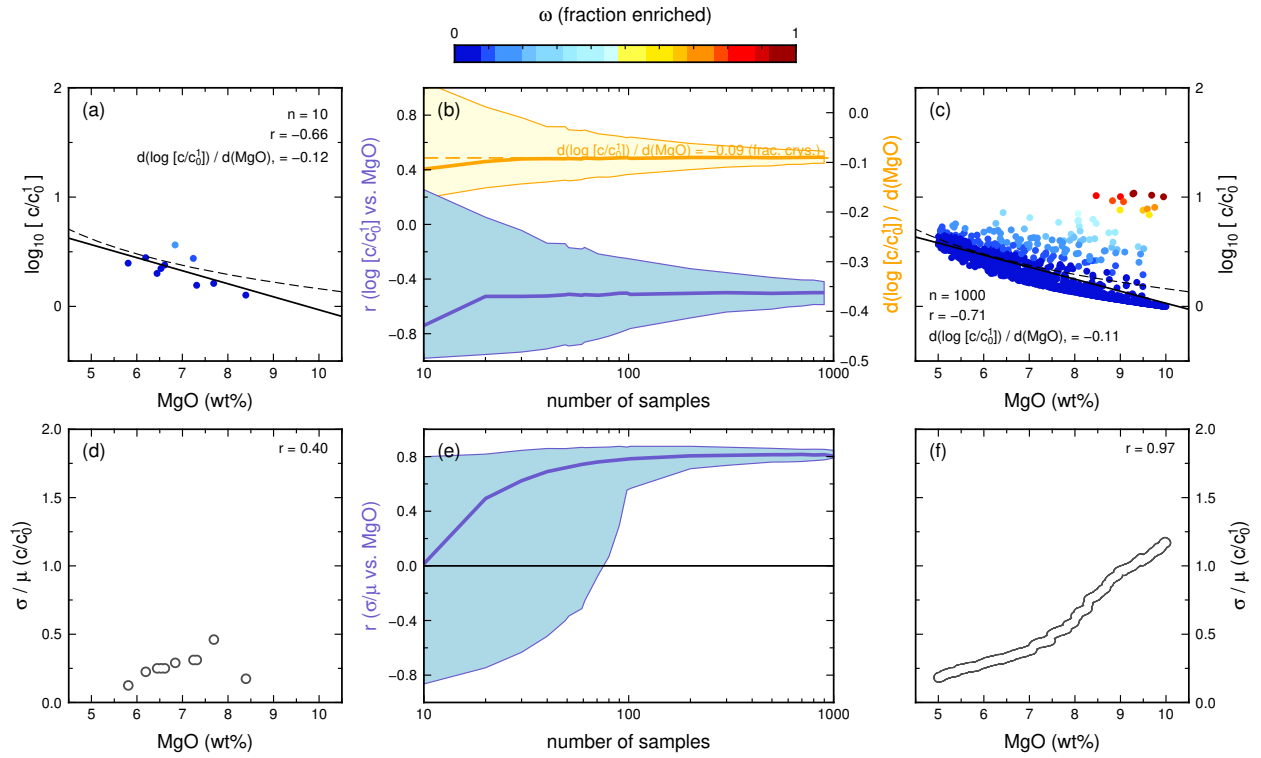
Figure A2: The influence of sample abundance on the reliability of estimates of gradient $(d(\log[C/C_0^1])/d(\mathrm{MgO}))$ and intercept in trace element–MgO space. In (a) an endmember case is shown, where a synthetic dataset has been produced drawing 10 samples (n = 10, the bulk starting composition $\omega_2 = 0.05$ and the enriched to depleted melt concentration ratio $C_0^2/C_0^1 = 10$). Points are plotted normalised to the concentration of C in the primitive depleted melt (C_0^1) and are coloured by the contribution of enriched melt ($\hat{r}_2$) in the mixture. The regression fitted to these data is shown as the solid black line, and the reference fractionation trend is shown as the dashed line starting from the mean composition of the primitive melts. A sweep across synthetic datasets of different sample sizes (n = 10–1000) is shown in (b). At each value of n, 2000 synthetic datasets have been produced and for each a gradient and intercept calculated. The median values of the gradient and intercept calculated at each n are shown as thick orange and blue lines respectively. Shaded regions around these lines record the 95% envelope of calculated gradients and intercepts. The other endmember case of high sample abundance is shown in (c), where n = 1000. In (d), (e) and (f), the corresponding profiles of geochemical variability (measured as standard deviation σ normalised to the mean composition μ) as function of MgO are plotted. The correlation coefficient r gives the correlation between σ/μ and MgO, and in (e) this is the parameter plotted as a function of n.

42

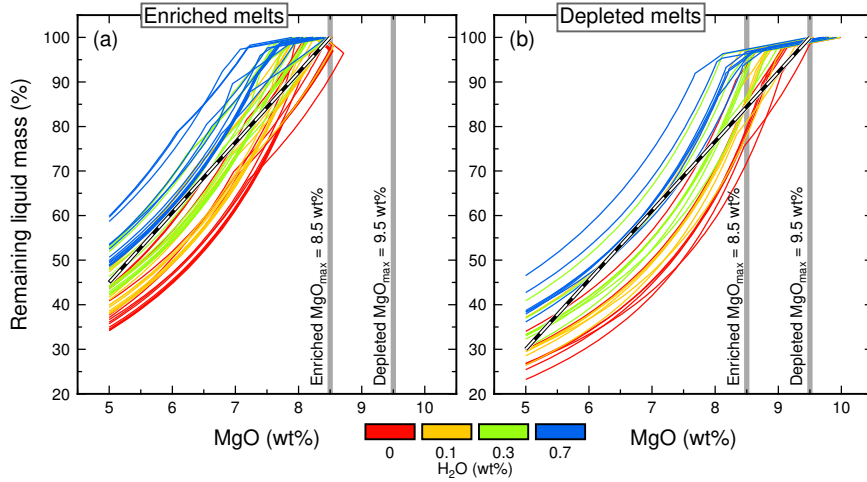*Mass loss during MORB differentiation: $K_d(\text{MgO})$*

Figure A3: The mass loss during fractional crystallisation of enriched melts (a), and depleted melts (b). Solid curves represent the fractionation path of individual endmember enriched and depleted melts, coloured by the water content used in calculations. Calculations investigated a range of water contents, from 0 to 0.7 wt%. The black dashed line represents the liquid mass–MgO relationship used in the mixing and fractionation calculations, starting at the inferred primitive MgO of each endmember (grey vertical bars: 8.5 wt% and 9.5 wt% MgO for enriched and depleted melts respectively). Starting melt compositions have been selected from their position in MgO–trace element space (Fig. 10 (a)). All calculations performed using Petrolog version 3 (Danyushevsky and Plechov, 2011), with the olivine, clinopyroxene and plagioclase models of Danyushevsky (2001), a fixed pressure of 2 kbar, and assuming a closed system for oxygen with 12% of the iron as ferric iron.

For fractional crystallisation models the fundamental variable driving trace element enrichment is the remaining liquid mass (X, equation 1), and ideally we would discuss over- or under-enrichment of trace elements in the context of trace element–X plots. However, with no direct measure of how much mass has been lost from the parental liquid in natural samples, we instead take the concentration of a compatible element as a proxy for this, typically MgO, referenced to an estimate of the initial MgO. In this trace element–MgO space, the appearance of trace element over-enrichment is predicated upon knowing the relationship between mass loss from the magma and MgO. This parameter is described by the effective partition coefficient for MgO between solid and liquid, $K_d(\text{MgO})$. As illustrated in Figure 1 of Coogan and O'Hara (2015), as $K_d(\text{MgO})$ drops (i.e. MgO becomes more incompatible in the crystallising assemblage) fractionation paths in incompatible trace element–MgO space steepen ($d(\log[\text{C}/\text{C}_0^1])/d(\text{MgO})$ becomes more negative), as more mass has to be extracted to achieve a given decrease in MgO. $K_d(\text{MgO})$ is therefore a critical parameter in modelling trace element evolution during differentiation.

In our model, given parental MgO contents (identified previously) and a final MgO (taken to be 5 wt%) we need to make a choice for the value of $K_d(\text{MgO})$ over this interval, and by implication how much mass is lost from the magma. To identify appropriate $K_d(\text{MgO})$ values we have modelled the fractional crystallisation of endmember enriched and depleted melts using Petrolog (Danyushevsky, 2001; Danyushevsky and Plechov, 2011). For these calculations we varied the water content in the starting melts between 0 and 0.7 wt%, as our analysis of the Gale et al. (2013a) dataset in previous sections only provided estimates of the endmember melts' lithophile trace element and major element composition. The differentiation trends of remaining liquid mass vs. MgO for enriched and depleted melts are shown in Fig. A3, coloured by their water content (red is anhydrous, to blue as wet). For enriched melts with a starting MgO close to 8.5 wt%, differentiation to 5 wt% MgO lowers the mass of the magma from between ~ 40–65%, whereas over the same interval depleted melts with a primary MgO of ~ 10 wt% have lost between ~ 55–75% of their mass. The effect of water on both enriched and depleted melts is to reduce the amount of mass loss for the given drop in MgO. This occurs because water suppresses plagioclase crystallisation and hence protracts the period of olivine
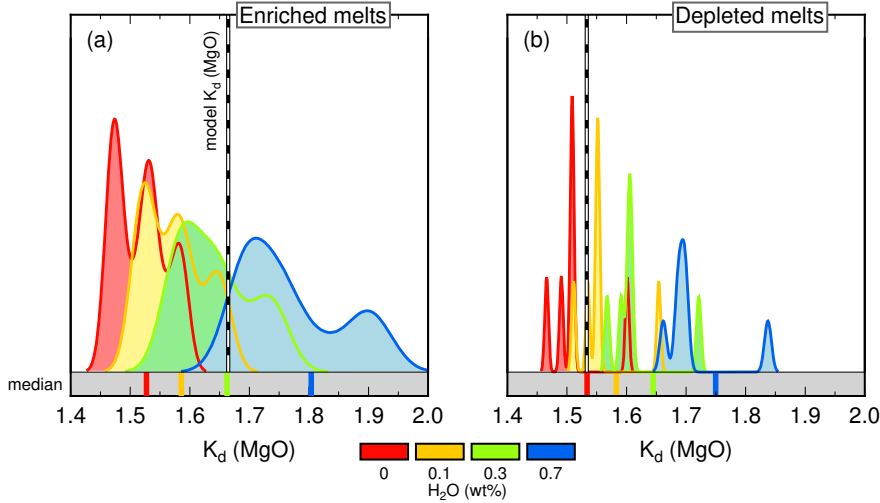
Figure A4: Kernel density estimates of the effective $K_d(\mathrm{MgO})$ during fractional crystallisation of each of the enriched (a) and depleted (b) endmember melt compositions show in Fig. A3. Each distribution is coloured according to the water content used in the fractionation calculation. Vertical coloured bars below the kernel density estimates show the median values of $K_d(\mathrm{MgO})$ for each distribution. The vertical black dashed lines mark the $K_d(\mathrm{MgO})$ implied by our assumption of a linear mass loss–MgO relationship (as shown in Fig. A3). These model $K_d(\mathrm{MgO})$ are 1.66 and 1.53 for the enriched and depleted melts respectively, and correspond closely to the median values obtained from Petrolog modelling for an enriched melt with 0.3 wt% water and an anhydrous depleted melt.

only crystallisation (Danyushevsky, 2001). In choosing values of $K_d(\mathrm{MgO})$ for our model we are therefore implicitly making a statement about how wet the enriched and depleted magmas are.

From the results of Fig. A3 for each magma we have calculated an effective $K_d(\mathrm{MgO})$ over the crystallisation interval, and plotted these as kernel density estimates in Fig. A4. The effective $K_d(\mathrm{MgO})$ for these calculations range from 1.45 to 1.95 and as expected vary systematically with water content, with the highest $K_d(\mathrm{MgO})$ in the wettest magmas. To select an appropriate $K_d(\mathrm{MgO})$ from the distributions shown in Fig. A4, we can use estimates of the water content in enriched and depleted melts. Saal et al. (2002) showed that the water content of primitive depleted melt inclusions is around 0.06 wt%, falling between our calculated anhydrous case (red) and low-water case (0.1 wt% H_2O, orange in Fig. A4). If we take this as an estimate of the water content of primitive depleted basalts than an appropriate estimate of $K_d(\mathrm{MgO})$ is 1.53, lying between the anhydrous and low-water distributions in Fig. A4 (b). If we also assume that the ratio H_2O/Ce is approximately constant between enriched and depleted basalts, which it appears to be to a first order (e.g. Hartley et al. (2015)), then we can use the Saal et al. (2002) water value of 0.06 wt% and scale up proportional to the enrichment of Ce in the enriched melt relative to the depleted melt. We constrained the relative enriched to depleted melt Ce ratio (Fig. 11), giving a value of ~ 5, and therefore an inferred water content of ~ 0.3 wt%. The median $K_d(\mathrm{MgO})$ for enriched melts with 0.3 wt% H_2O in our calculations is 1.66, and this is the value we take for modelling.

Using these values of $K_d(\mathrm{MgO})$ and our simplification that mass loss is linear with MgO over the studied range, we can calculate the final liquid mass from crystallisation of enriched and depleted basalts. These modelled trajectories are shown as black dashed lines in Fig. A3. The enriched melts in our model undergo a 55% mass loss on differentiating to 5 wt% MgO (i.e. $X_{max}^{(2)} = 0.55$), whereas the depleted melts loose 70% of their mass (i.e. $X_{max}^{(1)} = 0.70$). The mass loss used in calculating the fractional crystallisation trajectory for any given synthetic melt (X_{max}, using equation 13), is then calculated from a weighted addition of the enriched and depleted melt contributions to it, r_1 and r_2, using equation 4.

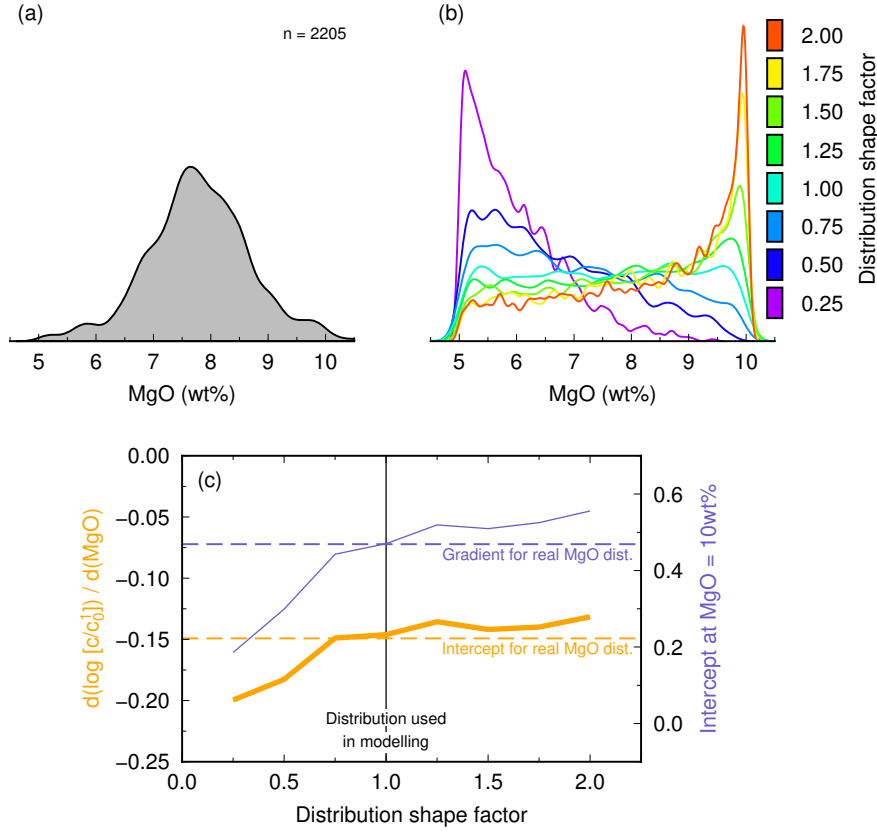*MgO distribution: effect on calculated gradients*

Figure A5: The effect of the MgO distribution of data on the calculated trace element–MgO gradients ($d(\log[C/C_0^1])/d(\mathrm{MgO})$). (a) kernel density estimate of the distribution for the natural MORB dataset used in this study. In (b) eight synthetic MgO distributions have been produced, formed of the same number of points as in the real dataset, but with variable shape (or skew) away from a uniform distribution (shape factor = 1). The calculated gradients (solid orange line) and intercepts (solid blue line) for suites of synthetic melts corresponding to the MgO distributions in (b) are shown in (c) as a function of the distribution shape factor. The horizontal dashed lines show the gradient and intercept obtained using the natural MgO distribution in (a) to produce the synthetic dataset. Using the natural MgO distribution to produce a fractionated and mixed dataset gives nearly identical results in terms of a linearly regressed gradient and intercept to the uniform distribution. Synthetic melts were generated using $C_0^2/C_0^1 = 10$ and $\omega_1 = \omega_2 = 0.5$, and assuming a perfectly incompatible trace element.

A potentially important factor when calculating fractionation gradients ($d(\log[C/C_0^1])/d(\mathrm{MgO})$) of real sample distributions is the MgO content of the samples. As is apparent in the schematic of fractionation in Fig. 2, and from equation 1, if mass loss from the fractionating magma remains linear in MgO (as it approximately does over the 10–5 wt% MgO range considered here, Fig. A3), then the data gradient in incompatible trace element–MgO space will steepen. The result is that regression gradients will appear more negative as the mean MgO of the sample distribution decreases. This will naturally effect the incompatible elements the most, and compatible elements the least. Therefore, in comparing $d(\log[C/C_0^1])/d(\mathrm{MgO})$ from synthetic datasets to natural datasets (or comparing between natural datasets), it is important to account for the MgO distribution of the data.

To ensure that our choice of MgO distribution for the synthetic calculations is not systematically offsetting our results from the natural data, we have tested a number of different MgO distributions for their effect on gradient and intercept. The effect of varying the sample abundance weighting between high and low MgO is illustrated in in Fig. A5, where from each synthetic distributions we have calculated a gradient and intercept for the corresponding trace element–MgO dataset. The change in gradient as the distribution is weighted

from low to high MgO is ~ 0.05, which is significant compared to the ~ 0.13 change between the most compatible and incompatible elements in the natural dataset (Fig. 14). We can also use the distribution of MgO in the natural samples (Fig. A5 (a)) to calculate a gradient and intercept, these are shown in Fig. A5 (c) as horizontal dashed lines. The gradient and intercept calculated using the distribution of MgO in the natural samples crosses the synthetic distributions where they have a 'shape factor' of 1, i.e. when a uniform distribution is used. This shows that in taking a uniform distribution to randomly distribute synthetic samples across MgO, no bias is introduced with respect to the natural dataset. We have therefore used a uniform distribution when generating synthetic datasets throughout this study.

Understanding the lower MgO of enriched MORB compared with depleted MORB

The MgO–enrichment prediction from simple peridotite fractional melting
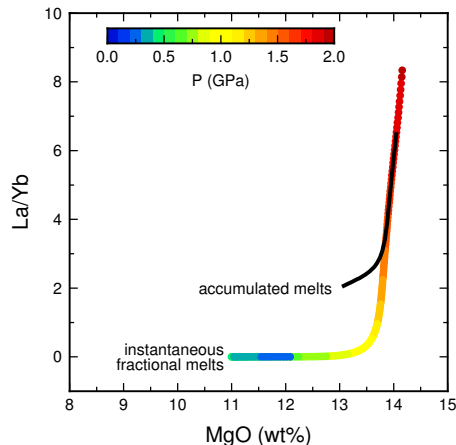

Figure A6: The composition of instantaneous fractional melts (coloured symbols) and 2D accumulated melts (black line) from a peridotite undergoing polybaric fractional decompression melting. The instantaneous melts are plotted as circles coloured by their pressure of formation. Calculated for a KLB-1 bulk composition with a potential temperature of 1340°C using the pMELTS software (Ghiorso et al., 2002; Smith and Asimow, 2005) and fixed K_d's from McKenzie and O'Nions (1991).

To understand the origin of the MgO difference we observe between enriched and depleted melts, it needs to be viewed in the context of what would be predicted from simple polybaric fractional fusion of a peridotitic source. We have calculated this reference case in Fig. A6, where La/Yb in instantaneous and accumulated fractional melts from a KLB-1 type peridotite are plotted as a function of their MgO. These results show that high-pressure low-degree melts are more enriched (have higher La/Yb) and have higher MgO, than lower pressure high-degree melts. This is the opposite trend to what we observe in natural MORB (Fig. 10). We therefore conclude that fractional melting of a homogeneous source does not on its own produce enriched melts with low MgO. Instead, either source lithological heterogeneity, or different phase relations during crystallisation, may account for the lower MgO of enriched basalts compared with depleted basalts. We further investigate this latter possibility below.

The latent heat buffering of enriched and depleted MORB differentiation

We previously showed evidence for the MgO of enriched melts being systematically lower than that of depleted melts. In addition to mantle lithological heterogeneity, we suggested that the phase relations of enriched, hydrous, basalts — even with otherwise identical major element compositions — would be such that for a given heat loss they will have a lower MgO than anhydrous melts. Here, we have quantified this hypothesis with thermodynamic calculations of basalt differentiation for a range of water contents (Fig. A7).

The curves in Fig. A7 (a) show the instantaneous enthalpy of fusion (ΔH_{fus}) for a single MORB composition, but with water contents ranging from anhydrous (red), to 0.7 wt% (blue). The clear effect of adding water is to reduce ΔH_{fus} of the basalt over the early stages of differentiation (10–8.5 wt% MgO). In Fig. A7 (b) we re-express the instantaneous enthalpy of fusion as the cumulative heat release of the magma due to crystallisation over the range 10–5 wt% MgO ($\sum[\Delta H_{fus}]$). Plotting $\sum[\Delta H_{fus}]$ against MgO demonstrates that wet magmas have early differentiation paths evolving significantly less heat than anhydrous magmas.

Water's effect on the heat evolved from differentiating magmas in Fig. A7, results from its suppression of the onset of plagioclase saturation. This means that hydrous magmas experience a longer period of olivine-only fractionation, which as olivine evolves less heat than subsequent multi-phase assemblages, produces a smaller ΔH_{fus}. Integrating ΔH_{fus} to give the heat evolved over the differentiation interval, we can see that the thermal buffering of wet magmas during their differentiation is significantly less than that of dry
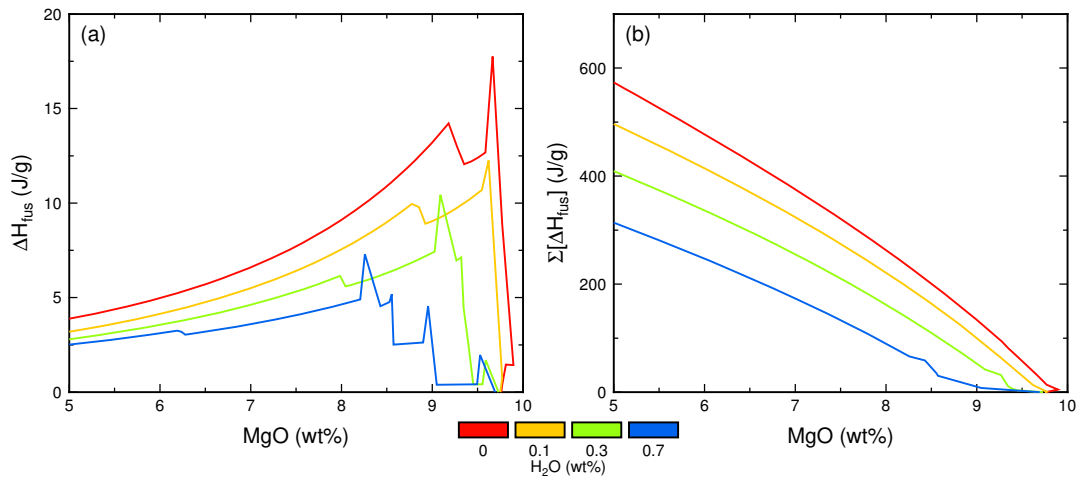
Figure A7: The heat released from a fractionally crystallising a primitive mid-ocean ridge basalt as a function of the magma MgO. Heat release is described in (a) as the enthalpy of fusion per degree of cooling per gram of system, ΔH_{fus}, and in (b) the cumulative heat release due to crystallisation over the differentiation interval is plotted, $\sum[\Delta H_{fus}]$. Four cases are studied, where the same basalt composition is variably hydrated, up to a maximum water content of 0.7 wt%. (b) Shows that for even small amounts of cooling, the hydrous magma has an MgO $\sim$ 1.5 wt% less than that of the anhydrous magma. Peaks in the heat release correspond to new phases coming onto the liquidus (Ghiorso, 1997). Calculations were performed with a pressure of 0.2 GPa and with oxygen buffered at FMQ-1 using the MELTS software (Ghiorso and Sack, 1995; Asimow and Ghiorso, 1998; Asimow et al., 2004; Smith and Asimow, 2005).

magmas. By the point that a wet magma has become multiply saturated, and so begins to buffer its cooling with latent heat release, it has already accrued an MgO deficit compared to dry magmas of between 0.6 and 1.5 wt%. We would therefore expect, at a given mid-ocean ridge heat flux, for hydrous magmas to have a lower MgO than anhydrous magmas. Given that enriched magmas are likely to be wetter than depleted magmas (e.g. Michael (1995)), this result naturally leads to the expectation that enriched magmas will be a low MgO mixing endmember during CMC processes in the crust.
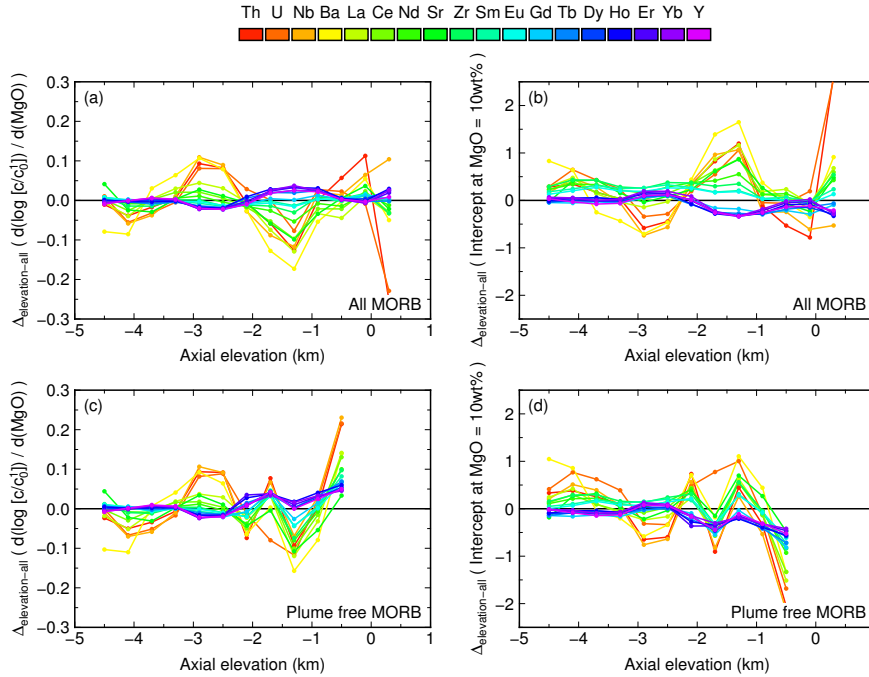
Axial depth as a proxy for melt supply

Figure A8: These plots assess whether there is any systematic relationship between the gradient of trace elements in trace element–MgO space and ridge axial elevation. Axial elevation is taken here as a proxy for melt supply, with the logic that all else being equal, a shallower axial elevation means higher mantle potential temperature, and therefore higher melt supply. In (a) and (b), the global MORB dataset of Gale et al. (2013a) has been sub-sampled according to ridge axial elevation in 450 m width bins and trace element–MgO gradients (a) and intercepts (b) calculated for a range of trace elements from samples in those elevation bins (lines coloured by element). The gradient ($d(\log[C/C_0^1])/d(\text{MgO})$) and intercept (at 10 wt% MgO) in that axial elevation range are then plotted with respect to the value obtained regressing the whole dataset without sub-division according to elevation (and as are such prefixed with Δ_{all}). In (c) and (d) this has been repeated, but with the data filtered against sampled derived from plume influenced sections of ridge (as defined by Gale et al. (2013a)).

The analysis carried out in the main text assumed that the primary control on magma flux to the ridge axis was spreading rate. Whilst this is likely true, a secondary control on melt flux will be mantle potential temperature, as melting of a hot mantle will increase the melt flux for a given spreading rate (McKenzie and Bickle, 1988). Although direct mantle temperature estimates are not available for each sample in the Gale et al. (2013a) database, we can use the depth of the ridge axis where the sample was collected as a positively correlated proxy for it (Klein and Langmuir, 1987). We have therefore separated the global MORB dataset into samples drawn from discrete ridge axis depth intervals (450 m wide) from -4500 to 450 m above sea level, and calculated gradients $d(\log[C/C_0^1])/d(\text{MgO})$ and intercepts (at 10 wt% MgO) for data in each bin (Fig. A8). Similarly to our findings in the main text for spreading rate, Fig. A8 shows that neither the steepness of trace element profiles nor their intercept vary systematically with ridge axial depth. If the over-enrichment of trace elements during differentiation was strongly melt flux sensitive we might instead expect systematic negative deviations in the gradients as axial elevation shallows. This is further evidence that trace element over-enrichment is possible in basalt suites erupted from cold deep ridge axes, which very likely lack a permanent axial magma reservoir.

Data sources

The sources of Icelandic whole-rock data used in Fig. 3 (a) & (b) are: Breddam et al. (2000); Maclennan et al. (2001b, 2003); Slater et al. (2001); Stracke et al. (2003); Nicholson et al. (1991); Kokfelt et al. (2006);

Koornneef et al. (2012); Chauvel and Hémond (2000); Maclennan et al. (2001a); Shorttle et al. (2013); Kokfelt et al. (2006); Breddam (2002); Hardarson and Fitton (1997); Chauvel and Hémond (2000); Sinton et al. (2005); Eason and Sinton (2009); Kokfelt et al. (2006); Koornneef et al. (2012); Hardarson and Fitton (1997); Gee et al. (1998a,b); Thirlwall et al. (2004); Peate et al. (2009).

Icelandic melt inclusion data used in Fig. 3 (c) are from: (Gurenko and Chaussidon, 1995; Slater et al., 2001; Maclennan, 2008a,b; Maclennan et al., 2003).